CONFIDENTIAL

NATIONAL AERONAUTICS AND SPACE ADMINISTRATION
CONTRACT NO. NASW-6

Quarterly Summary Report No. 38-5

for the period July 1, 1961 to September 30, 1961

GROUP 4
Downgraded at 3 year intervals; declassified after 12 years

JET PROPULSION LABORATORY
CALIFORNIA INSTITUTE OF TECHNOLOGY
PASADENA, CALIFORNIA

October 15, 1961

CONFIDENTIAL

GROUP 4
Downgraded at 3 year intervals; declassified after 12 years

Preface

This report is a quarterly summary of the research activities conducted by the Jet Propulsion Laboratory in the field of nondestructive testing of solid-propellant rocket motors. Section I details the progress in specific areas of research. An introduction to the problems and objectives of the program is given in QSR 38-1; a bibliography of the subject is presented in QSR 38-1, -2, and -3; Section I of QSR 38-4 presents a general description of the subject areas covered by the entire program.

The work reported herein is undertaken in partial fulfillment of the Advanced Research Projects Agency Letter Order No. 107-60, for the National Aeronautics and Space Administration.

W. H. Pickering, *Director*
Jet Propulsion Laboratory

This document contains information affecting the national defense of the United States, within the meaning of the Espionage Laws, Title 18, U.S.C., Sections 793 and 794, the transmission or revelation of which in any manner to an unauthorized person is prohibited by law.

Quarterly Summary Report No. 38-5

Copyright © 1961
Jet Propulsion Laboratory
California Institute of Technology

Contents

I. Physical Properties Studies 1

A. Motor Strain Testing, C. H. Lewis, Jr. 1

B. Viscoelastic Strain Analysis by Photoelastic Coating Technique, III, A. San Miguel 3

C. Polymer Degradation Mechanisms, J. D. Ingham and N. S. Rapp 23

References 27

I. Physical Properties Studies

A. Motor Strain Testing

C. H. Lewis, Jr.

A device to measure the width of a specimen continuously during a uniaxial tensile test has been fabricated and is in use. The device consists of two parts: a width measuring transducer and a platform mechanism upon which the transducer is mounted.

The transducer (Fig. 1) has two arms which touch either side of the specimen. One arm is fixed when in operation but can be adjusted to accommodate initial specimen widths from 0.350 to 1.020 inches. The other arm is spring loaded to physically track the specimen. The transducer assembly is free to move laterally so that, as the specimen contracts, the spring loaded arm causes the assembly to move sufficiently to keep the fixed arm in contact with the specimen. The position of the moving arm is measured through a lever by a linear potentiometer which is calibrated to read out width directly.

The platform (Fig. 2) displaces vertically at the rate of ½ the cross-head speed so that the transducer arms will track a given cross-section throughout a test. The platform is guided vertically on two rods which are mounted to the moving cross-head of the machine. The platform is held up by counterweights and is moved downward by the pulley system. If the measuring arms are positioned initially at the center of the specimen, they will follow this point as the cross-head moves. It is assumed that the initial center of the specimen remains midway between grips. This is not strictly true; by using photographs, however, the error has been found to be small.

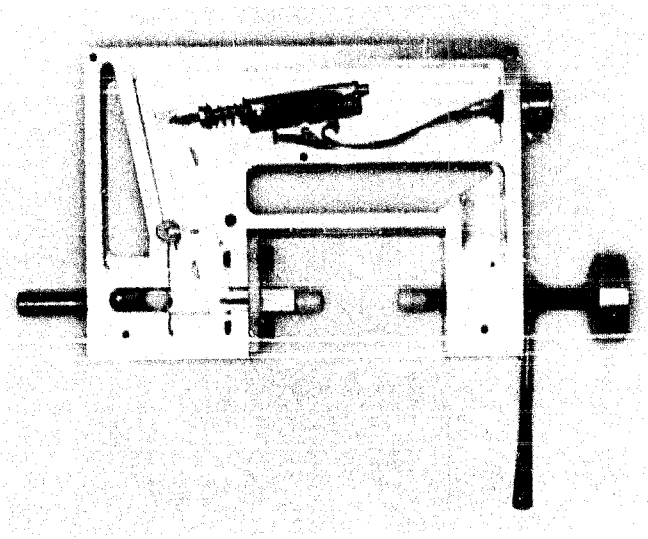

Figure 1. Width measuring transducer for uniaxial tensile tests

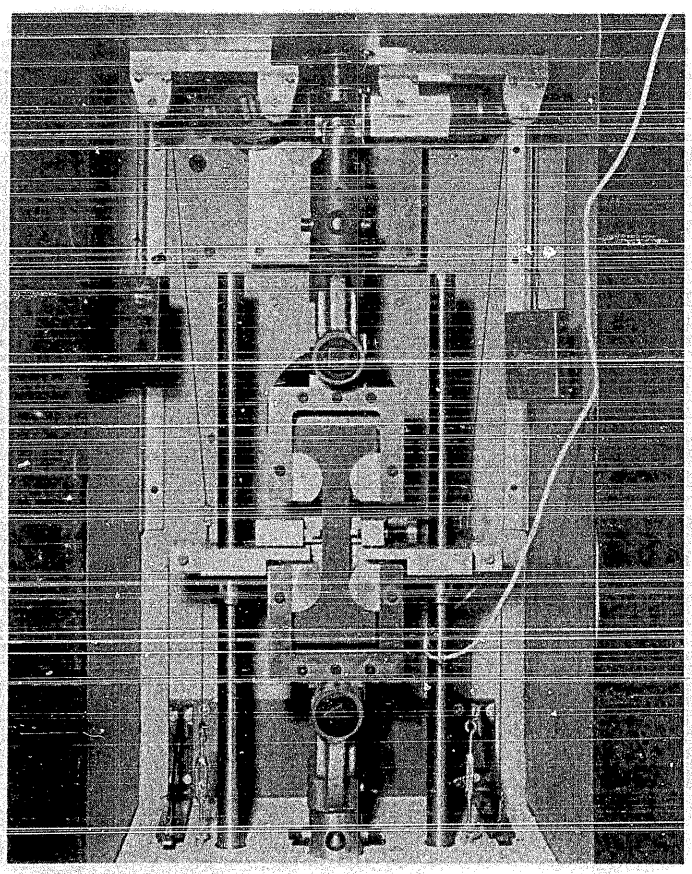

Figure 2. Uniaxial tensile testing device

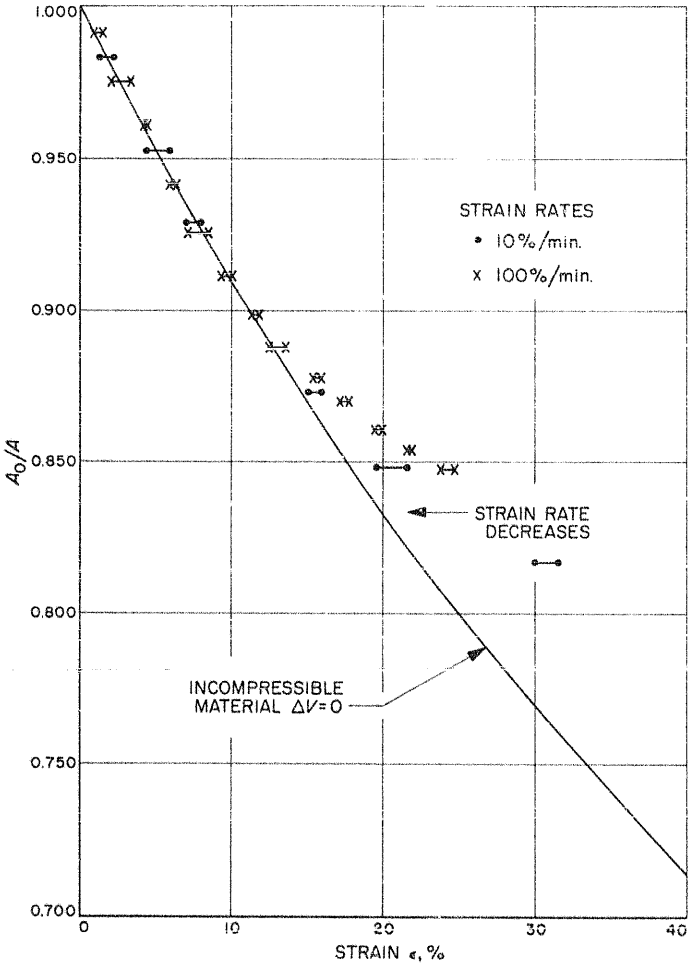

Figure 3. Variation of cross-sectional area with axial strain

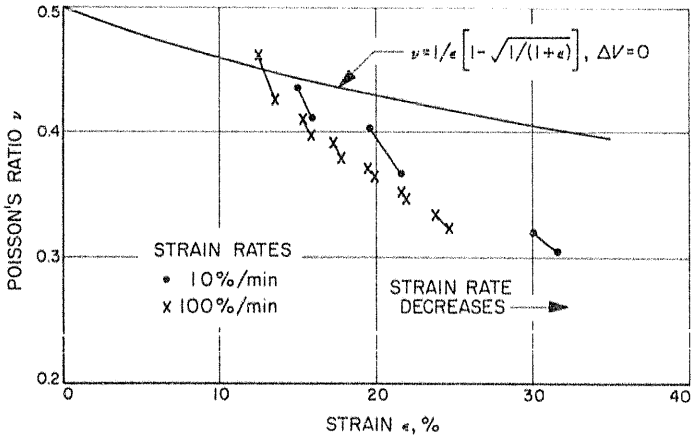

Figure 4. Variation of Poisson's ratio with axial strain

Steps are being taken to further refine the transducer. At present the device will measure a width of 1.000 inch to an accuracy of 0.0005 inch with a linearity of 1% over 0.100 inch of movement. Maximum deflection of the spring-loaded arm produces a 5-psi pressure on the specimen. It would be desirable to improve the linearity and to decrease the actuating force.

Figure 3 shows the variation in cross-sectional area for several tests in which the width was measured directly by use of photographs and the width measuring device. The two methods of measurement agree very well; however, the data reduction time is reduced almost 75% in using the width measuring device. For strains greater than approximately 10%, the actual variation in cross-sectional area appears less than that predicted assuming there is an incompressible material. This difference increases with strain and, apparently, strain rate. This difference can also be seen in the variation of Poisson's ratio (Fig 4).

The width device is part of a system being developed to measure true stress and actual strain directly from an axial tensile test. The axial strain measuring extensometer is still under development. The operation of the entire system will be described in a future issue of the *QSR*.

B. Viscoelastic Strain Analysis by Photoelastic Coating Technique, III

A. San Miguel

In *QSR 38-1* a method to measure viscoelastic strains in a motor grain at ambient temperature and quasi-static loading was presented in detail. Data for various grain configurations (boundary condition versus surface strain distribution) have now been recorded using the same basic equipment.

1. Apparatus and Procedure

Twenty grains were tested, which were divided into two major groups of ten. The first major group consisted of five large and five small free standing grains (Fig 5). The second major group consisted of five large and five small external radially restricted grains (Fig 6). The port geometries of all the grains are detailed in Figures 7

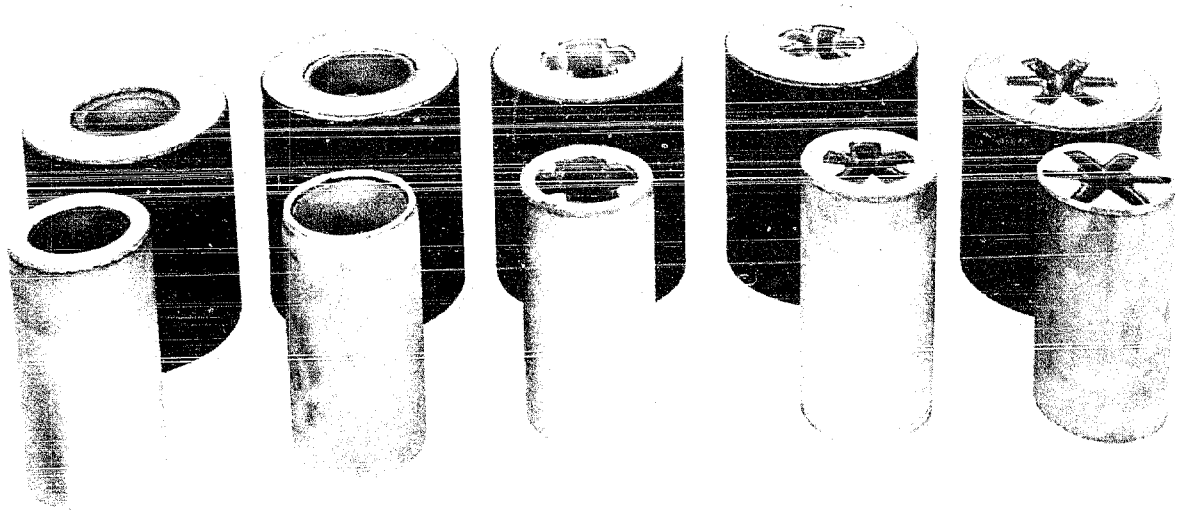

Figure 5. Free standing propellant grains

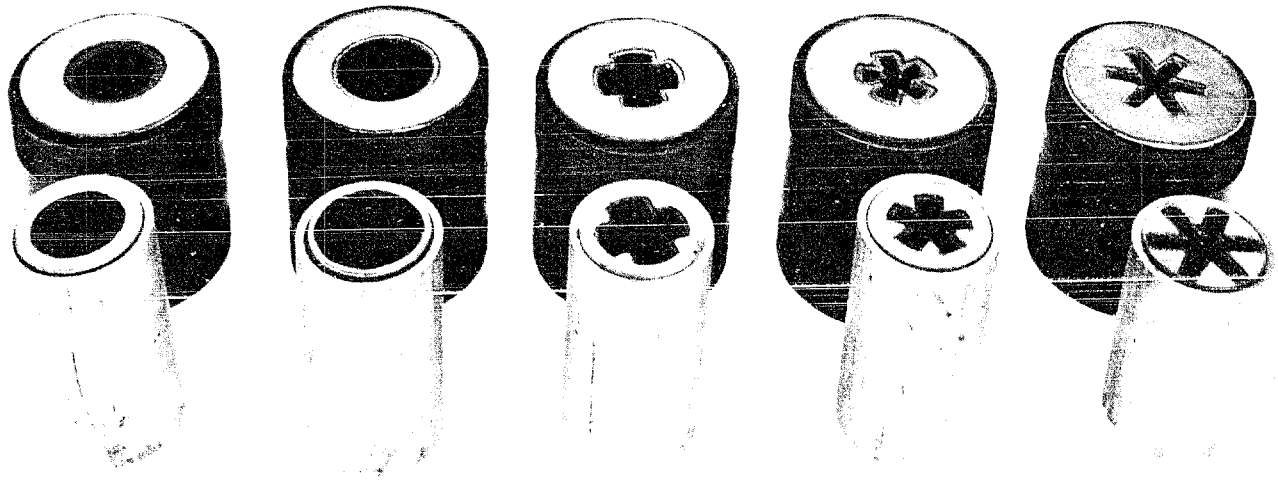

Figure 6. Fixed propellant grains

and 8. The difference in geometries between the large grains and the small grains is the outside diameter.

The material tested for the large grains was an inert formulation whose physical properties are similar to those of an operational polyurethane composite propellant. Due to casting difficulties, the small grain material did not cure properly and was tacky at the surface. These small grains were machined to give surface qualities similar to those of the large grains.

Internal pressurization was attained by using contoured latex bags sealed to a shaft at both ends. The loading system was the same as shown in *QSR* 38-4; the restrained grain consisted of the free grain inserted in a greased cylinder. Data were recorded on color film in the usual manner (Fig 9, and *QSR* 38-3).

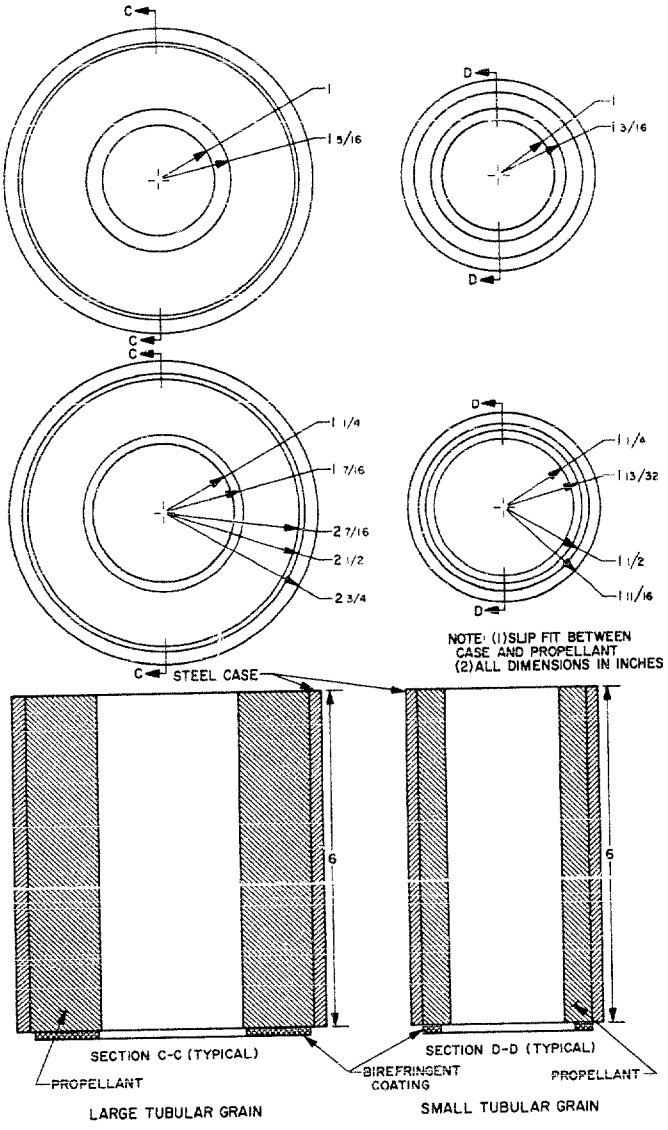

Figure 7. Large and small tubular grain geometries

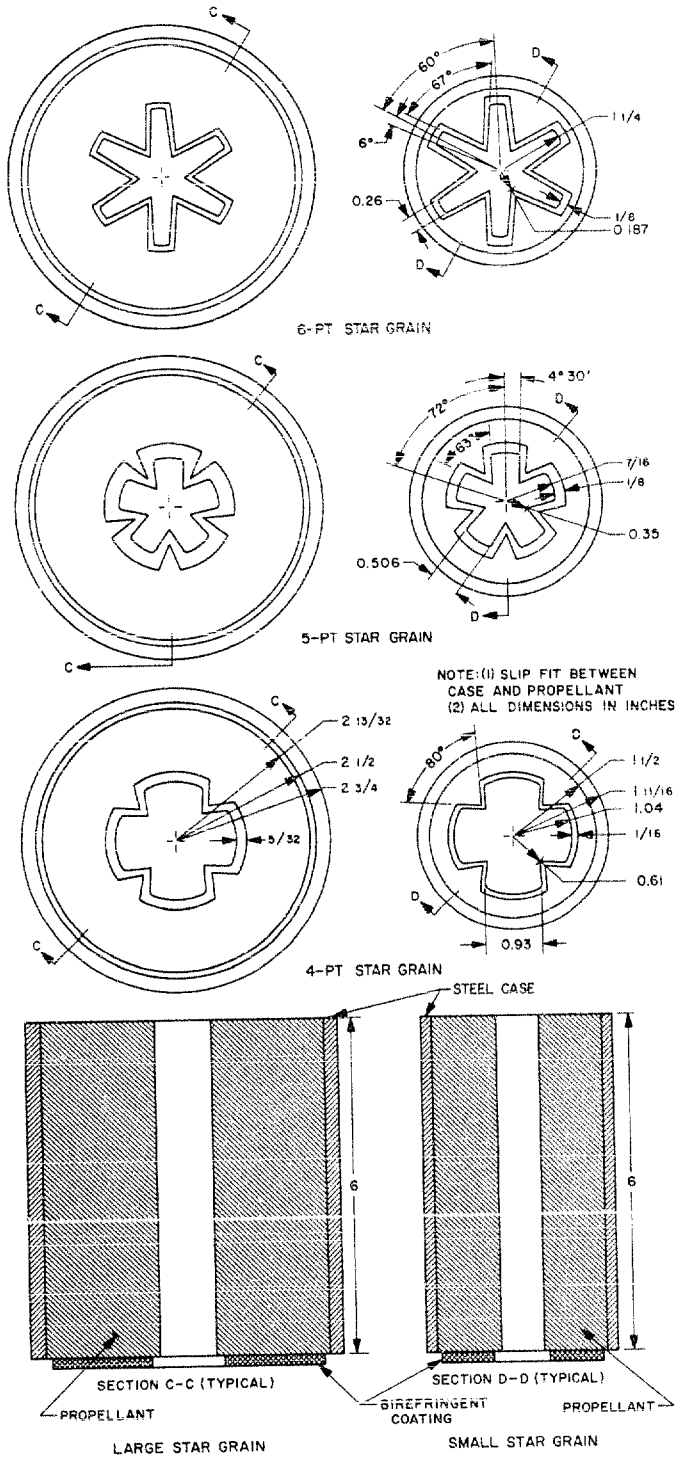

Figure 8. Large and small star grain geometries

2. Birefringent Coating Material

The sheets of birefringent coating resin were calibrated (*QSR* 38-3) and then cut to match their respective grains. Sufficient cut-back was allowed so that neither the end plates nor the cylinder wall would contribute spurious loading to influence the birefringent readings.

3. Data Reduction

Each large free grain was pressurized to 60 psi. Each large fixed grain was pressurized to 150 psi. The small free grains were pressurized to approximately 20 psi. (Note that the free grain six-pointed star was fractured at 13 psi.) The small fixed grains were pressurized to 100 psi (except for the six-pointed star which appeared to be about to fracture at 85 psi).

The photoelastic data were reduced from Figure 9 to Figure 10 for the various grain configurations. As in *QSR* 38-4, the geometries were traced from projected enlargements of a color film positive. All of the photographic data runs were performed in less than 7 seconds to minimize creep due to viscoelastic effects.

Following the same procedures established in *QSR* 38-3, the principal strains were determined at the web (Section A) and at the tooth (Section B). Figures 11 and 12 illustrate the graphical representation of the isochromatics for their corresponding geometry and loading (obtained m Fig 9 in the same manner used for Fig 10). In Figures 11 and 12, a plot in Cartesian coordinates of constant shear trajectories is superimposed upon the isochromatic plot. The nomograph and procedure used to separate the principal stresses are given in *QSR* 38-3. Table 2 in *QSR* 38-4 indicates the calculations that are necessary to reduce the difference of principal stresses $\sigma_1 - \sigma_2$ and σ_2 into the principal strains in the coating material.

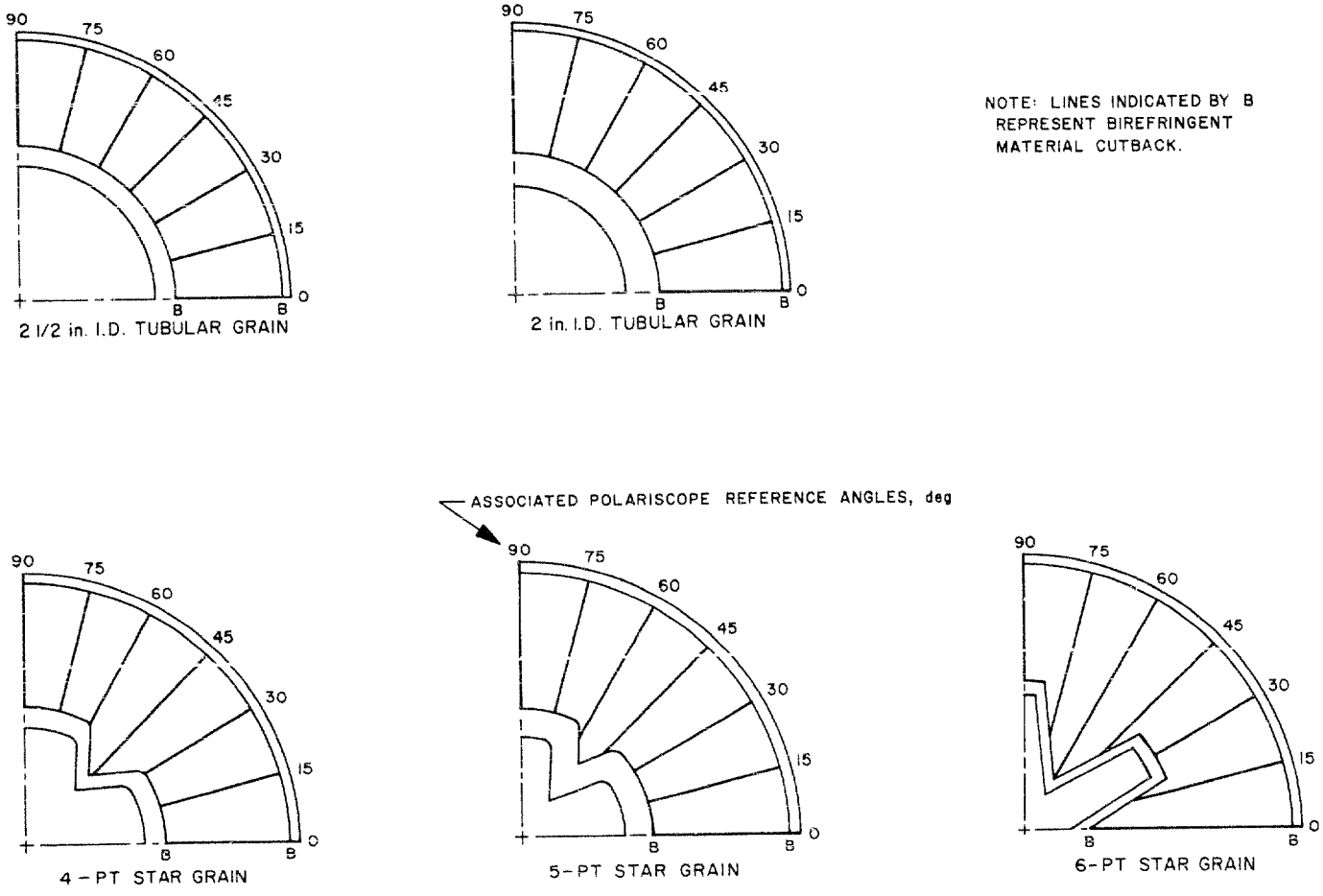

Figure 10. Graphical isoclinic interpretation of Figure 9

2-in I.D., TUBULAR, LARGE GRAIN
FIXED
FREE
2-in I.D., TUBULAR, SMALL GRAIN
FIXED
FREE
75
60
45
30
15

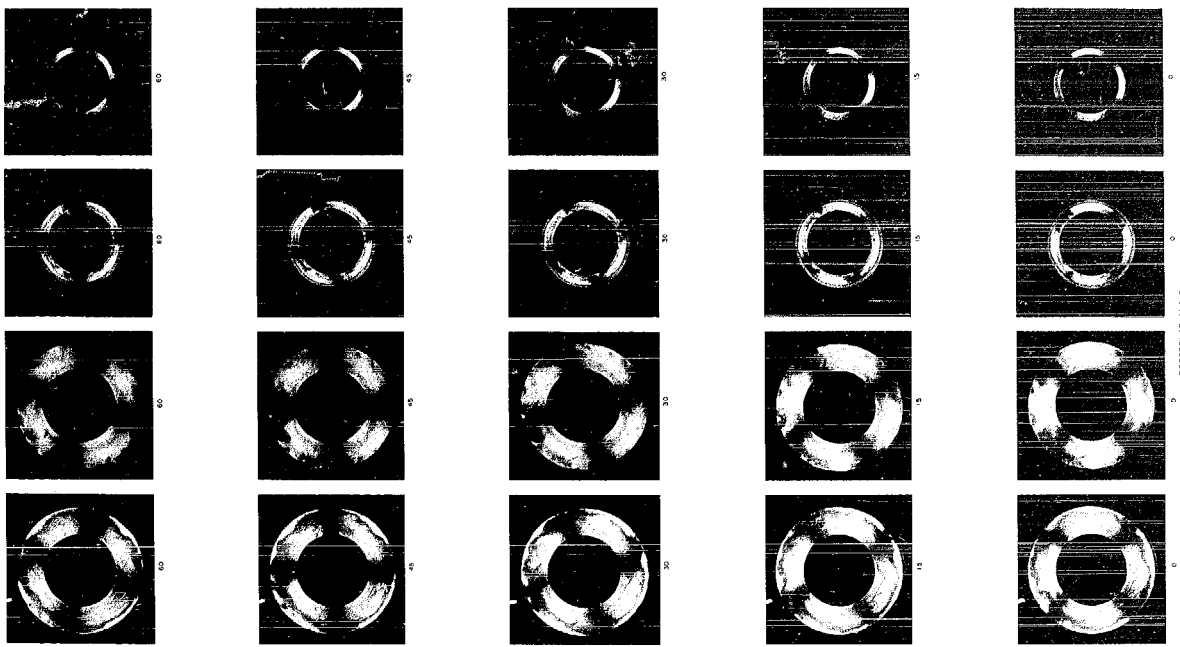

Figure 9. Photogenphic polariscope data

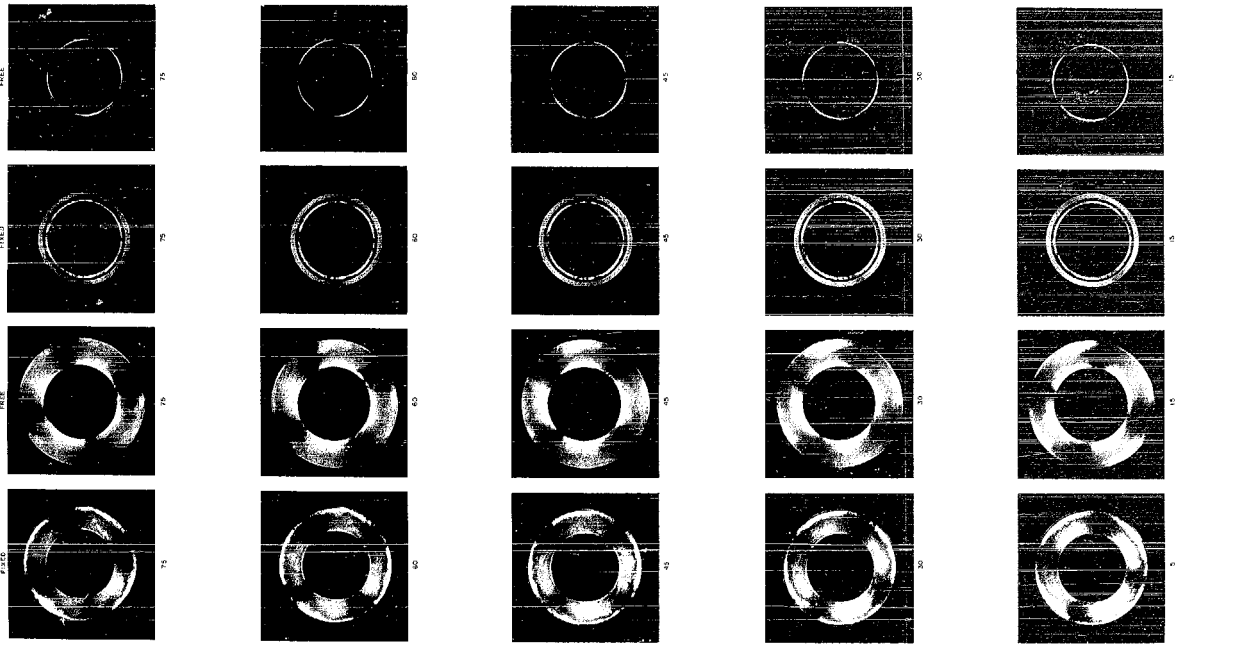
2 1/2-in I.D., TUBULAR, LARGE GRAIN
FREE
FIXED
2 1/2-in I.D., TUBULAR, SMALL GRAIN
FREE
FIXED
75
60
45
30
15
0

60
60
45
45
30
30
15
15
0
0
REFERENCE AXIS E. deg
0
Figure 9. Photographic polariscope data found.

FIXED 4-PT STAR, LARGE GRAIN
FREE
FIXED 4-PT STAR, SMALL GRAIN
FREE
75
60
45
30
15

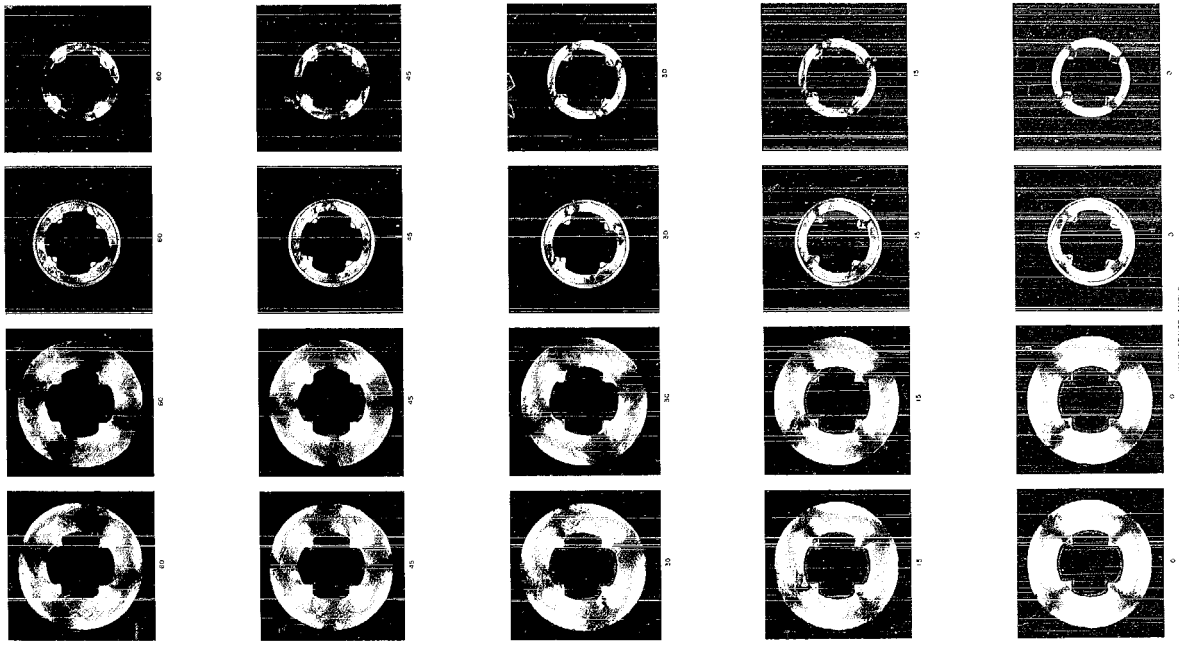

Figure 9. Photographic polariscope data (cont'd)

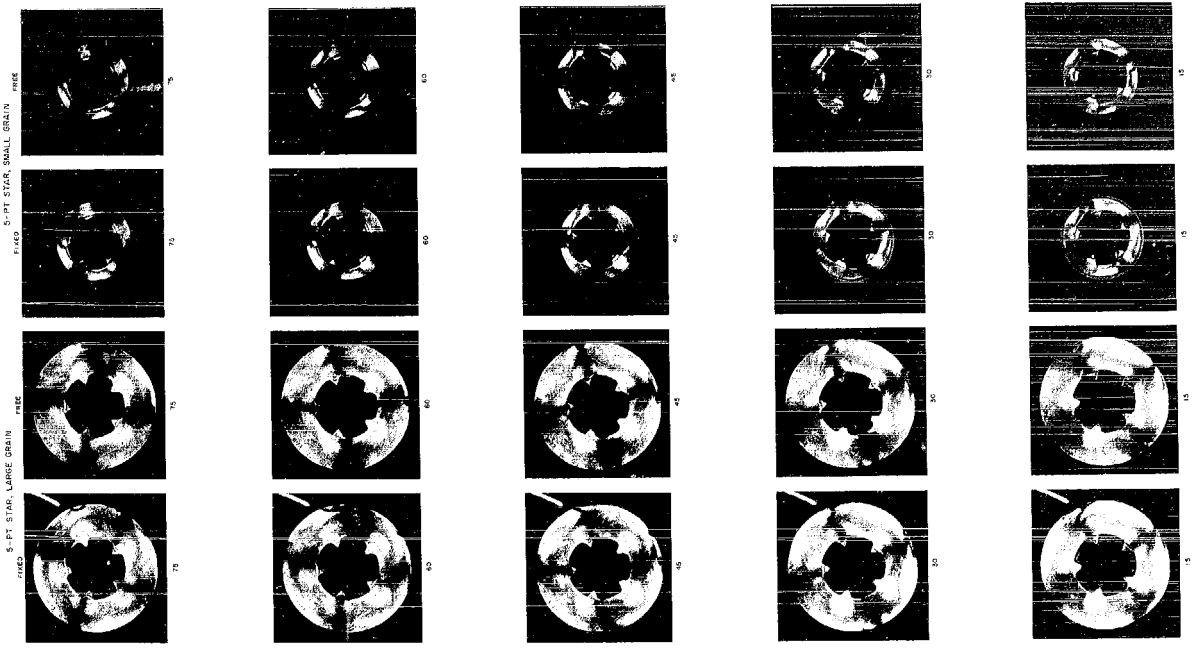
5-PT STAR, LARGE GRAIN
FIXED
FREE
5-PT STAR, SMALL GRAIN
FIXED
FREE
75
60
45
30
15

Figure 9. Photographic polarscope data (cont'd)

6-7" STAR, LARGE GRAIN
FREE
6-7" STAR, SMALL GRAIN
FIXED
DISINTEGRATED
75
75
75
60
60
60
45
45
45
30
30
30
15
15
15

Figure 9. Photographic polarioscope data (control)

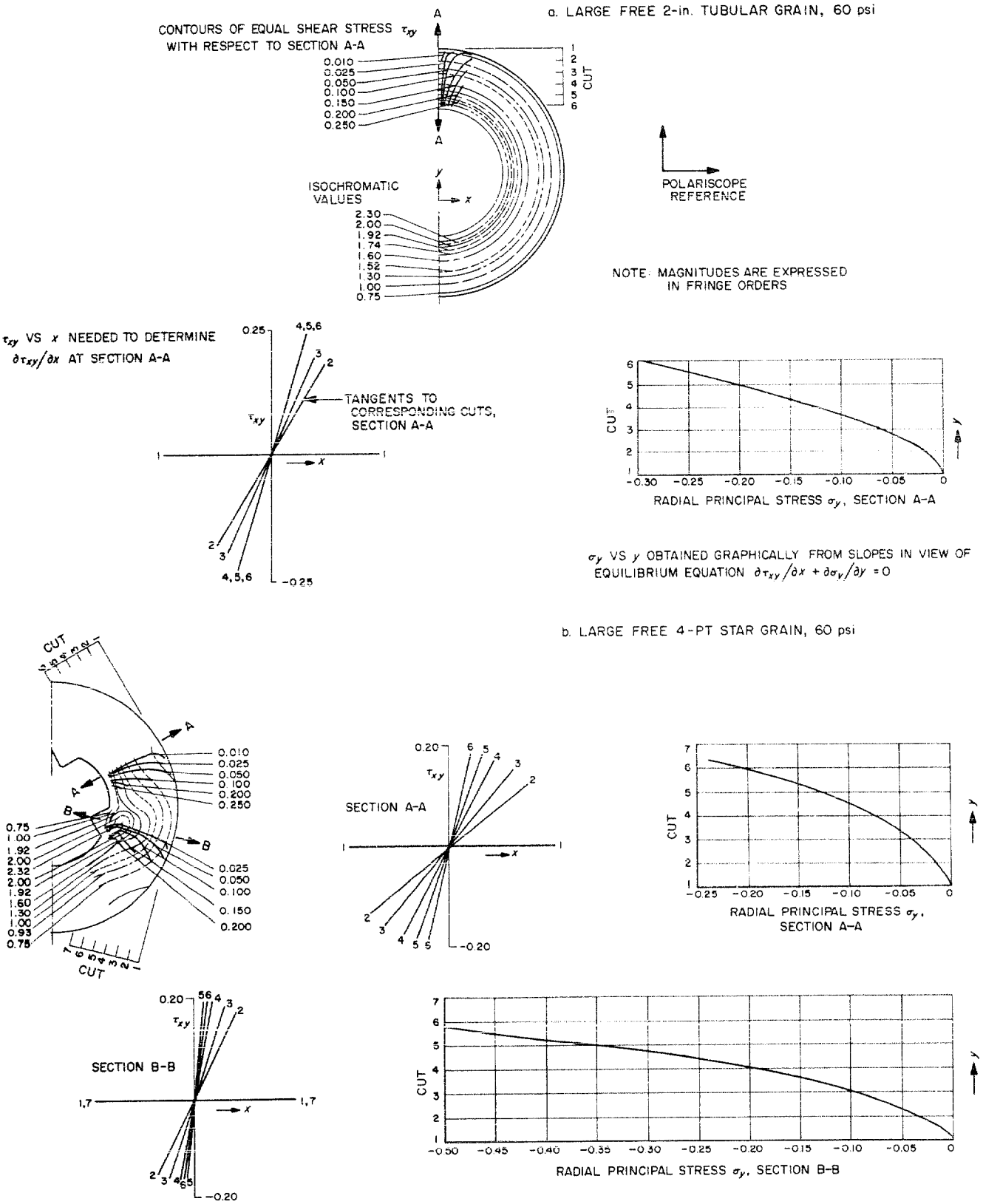

Figure 11. Isochromatic distribution and separation of principal stresses

c. LARGE FREE 5-PT STAR GRAIN, 60psi

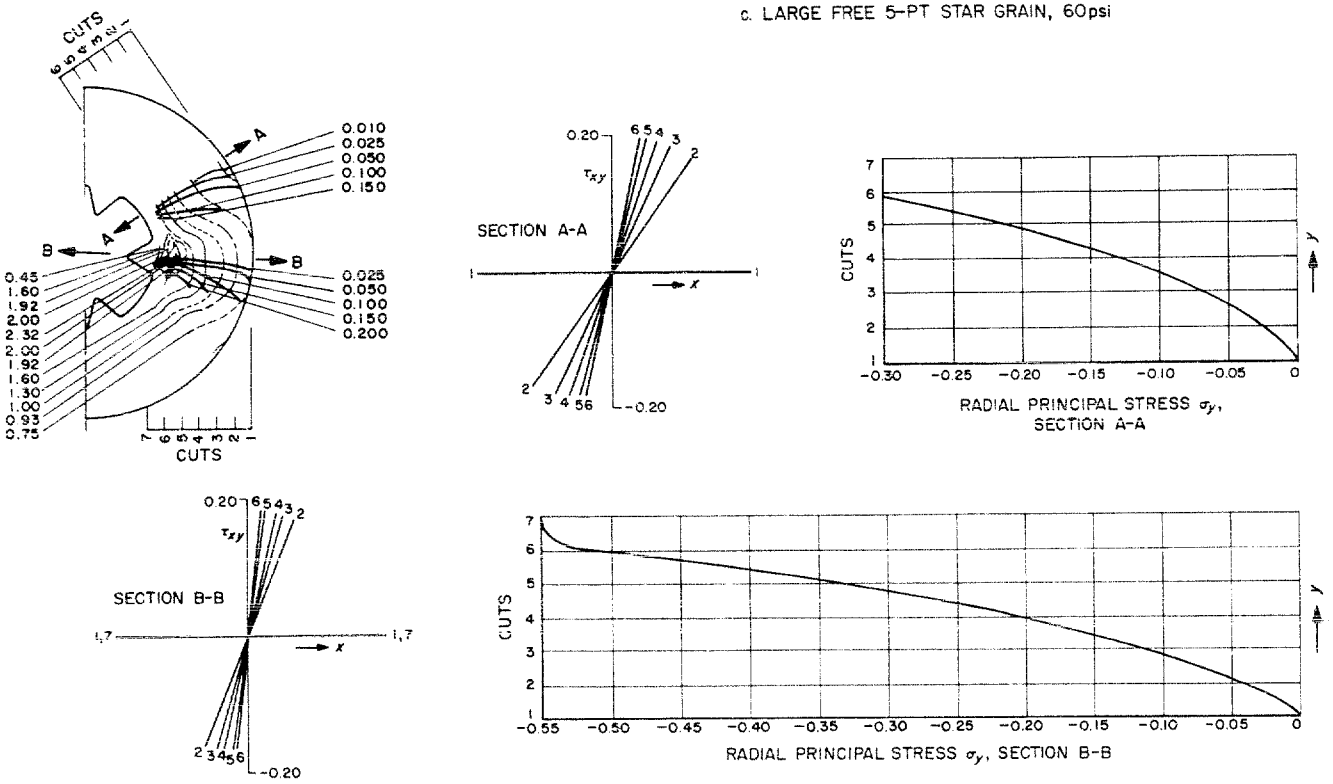

d. LARGE FIXED 2-in. TUBULAR GRAIN, 60 psi

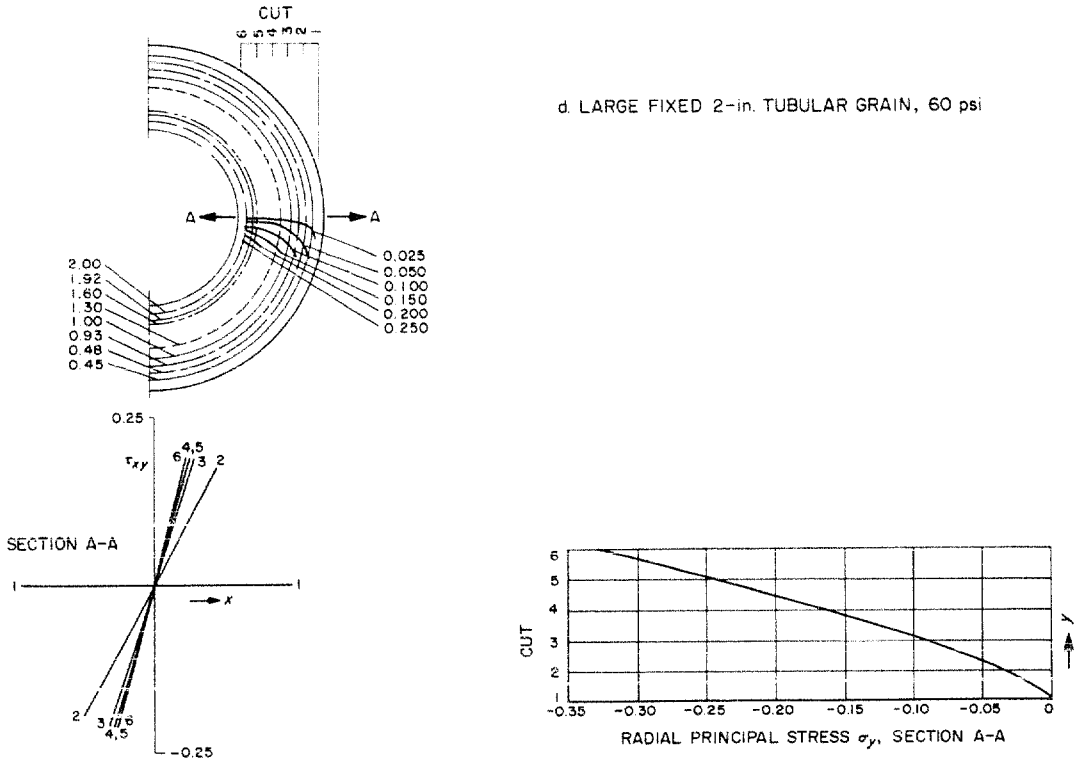

Figure 11. Isochromatic distribution and separation of principal stresses (cont'd)

e. LARGE FIXED 4-PT STAR GRAIN, 150 psi

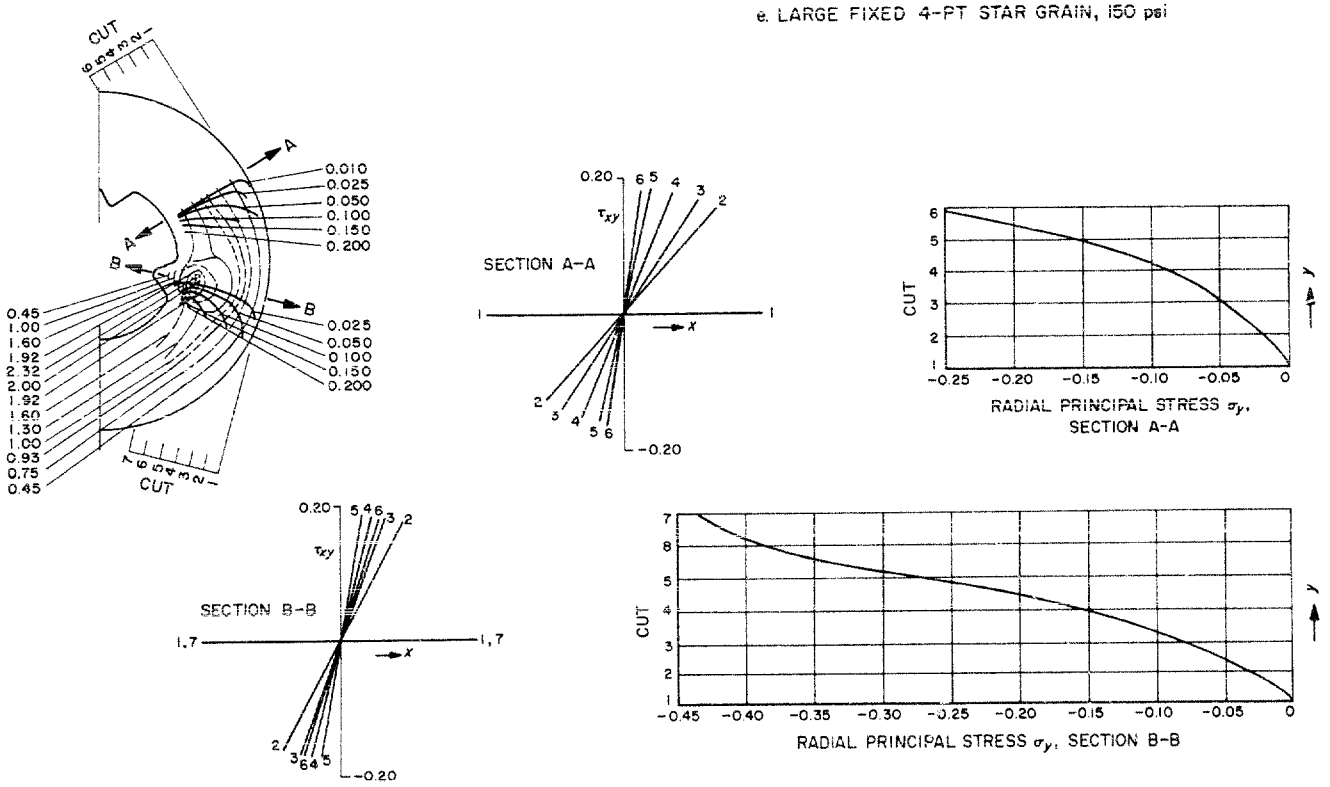

f. LARGE FIXED 5-PT STAR GRAIN, 150 psi

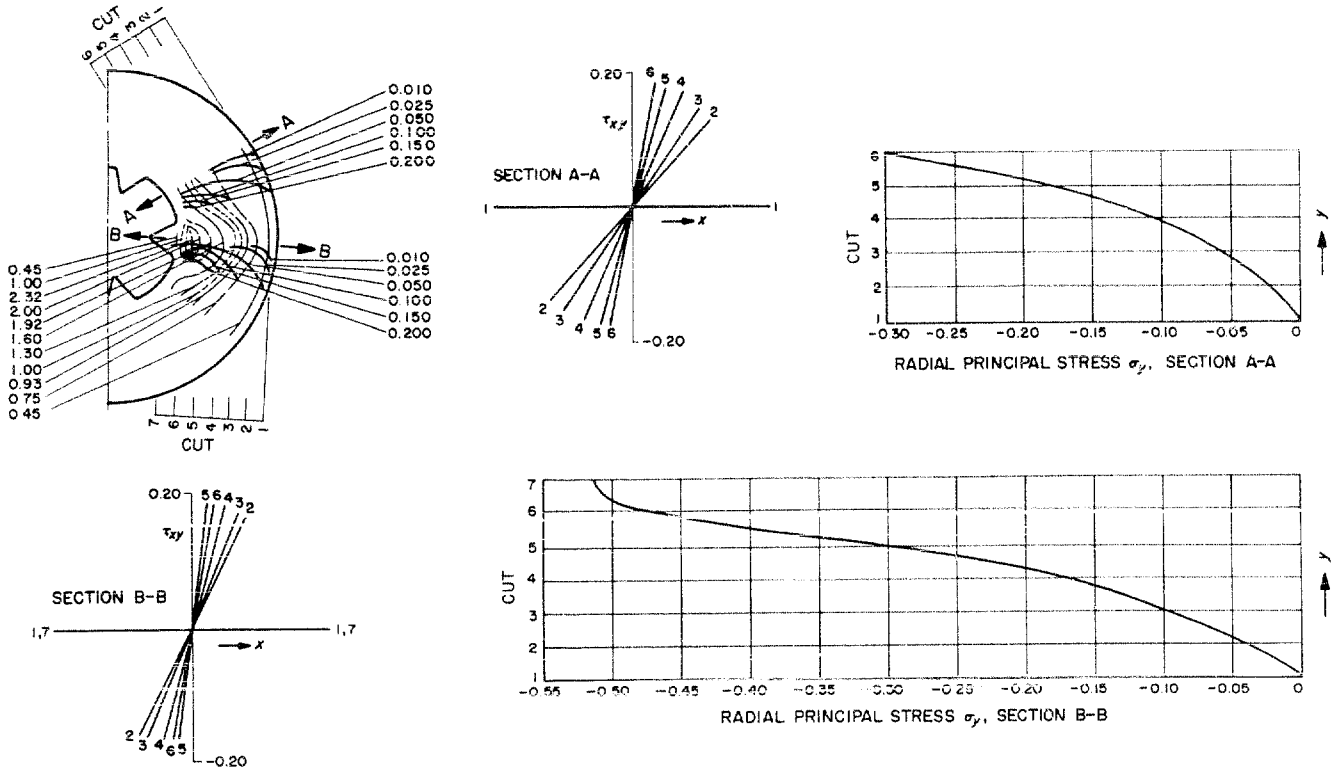

Figure 11. Isochromatic distribution and separation of principal stresses (cont'd)

g. SMALL FREE 2-in. TUBULAR GRAIN, 22 psi

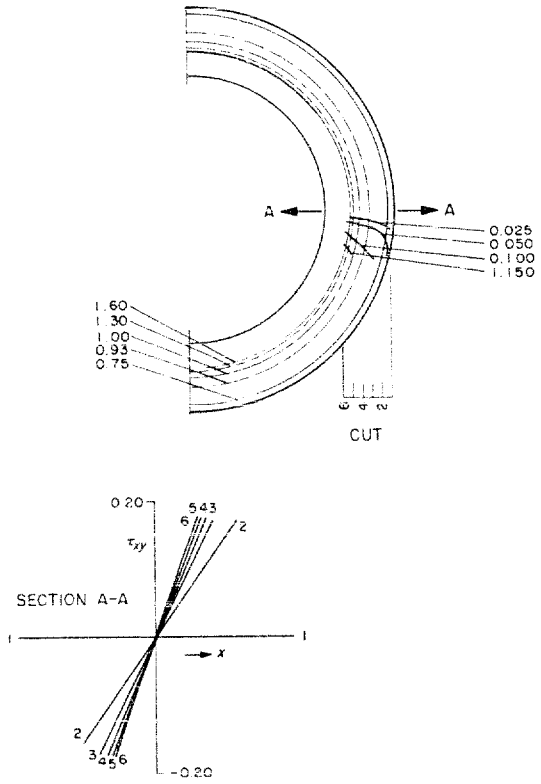

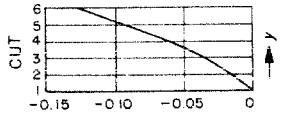

RADIAL PRINCIPAL STRESS σ_y, SECTION A-A

h. SMALL FREE 2 1/2-in. TUBULAR GRAIN, 8 psi

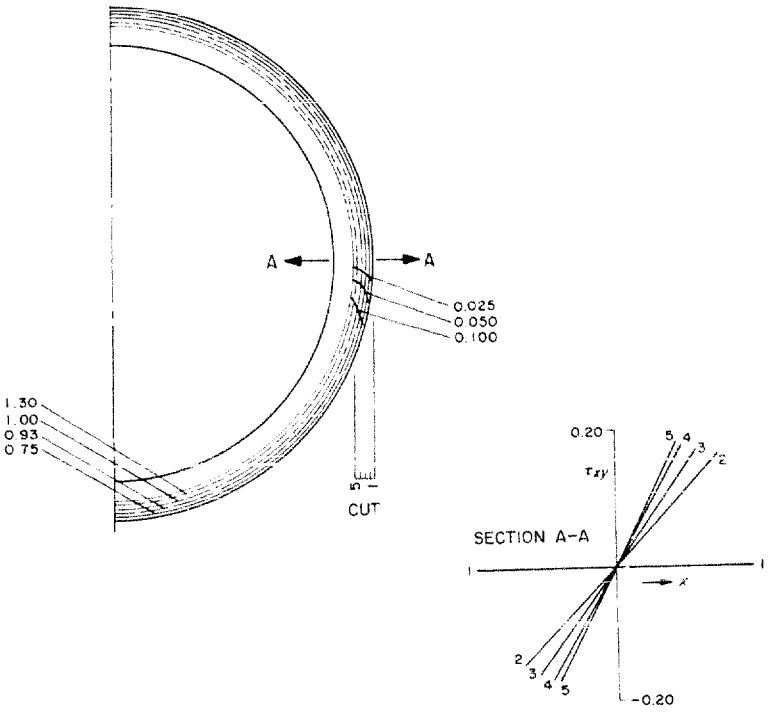

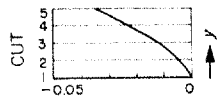

RADIAL PRINCIPAL STRESS σ_y, SECTION A-A

Figure 11. Isochromatic distribution and separation of principal stresses (cont'd)

i. SMALL FREE 4-PT STAR GRAIN, 36 psi

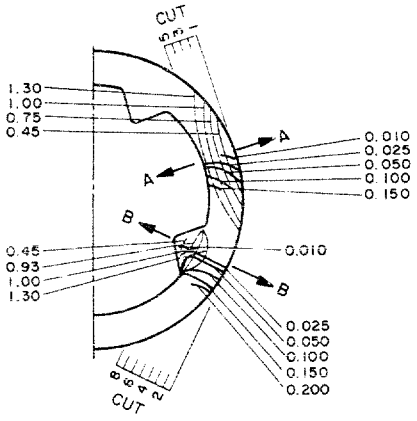

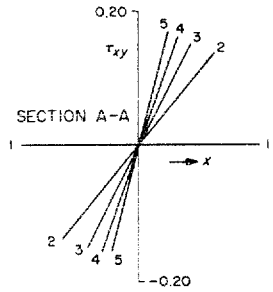

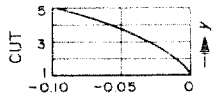

RADIAL PRINCIPAL STRESS σ_y, SECTION A-A

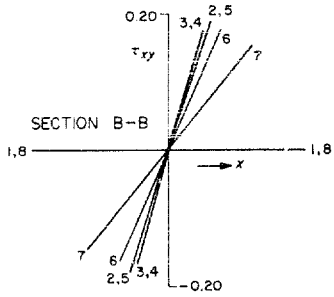

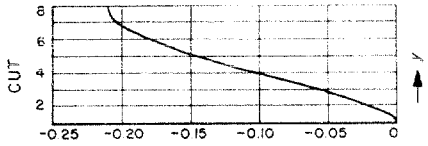

RADIAL PRINCIPAL STRESS σ_y, SECTION B-B

j. SMALL FREE 5-PT STAR GRAIN, 22 psi

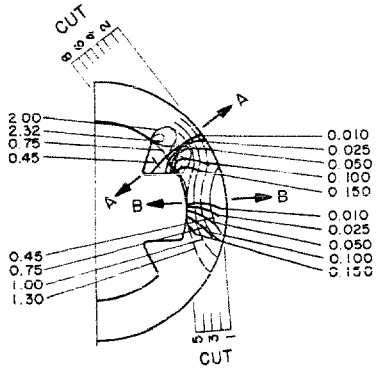

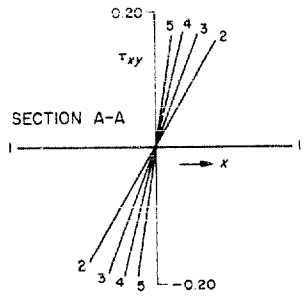

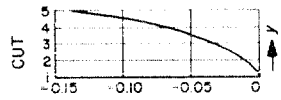

RADIAL PRINCIPAL STRESS σ_y, SECTION A-A

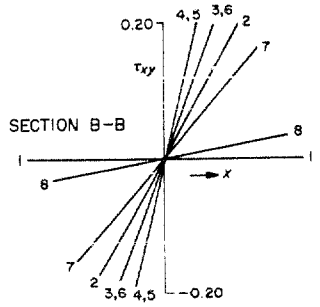

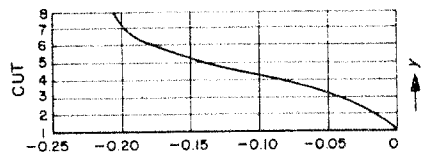

RADIAL PRINCIPAL STRESS σ_y, SECTION B-B

Figure 11. Isochromatic distribution and separation of principal stresses (cont'd)

k. SMALL FREE 6-PT STAR GRAIN, 13 psi

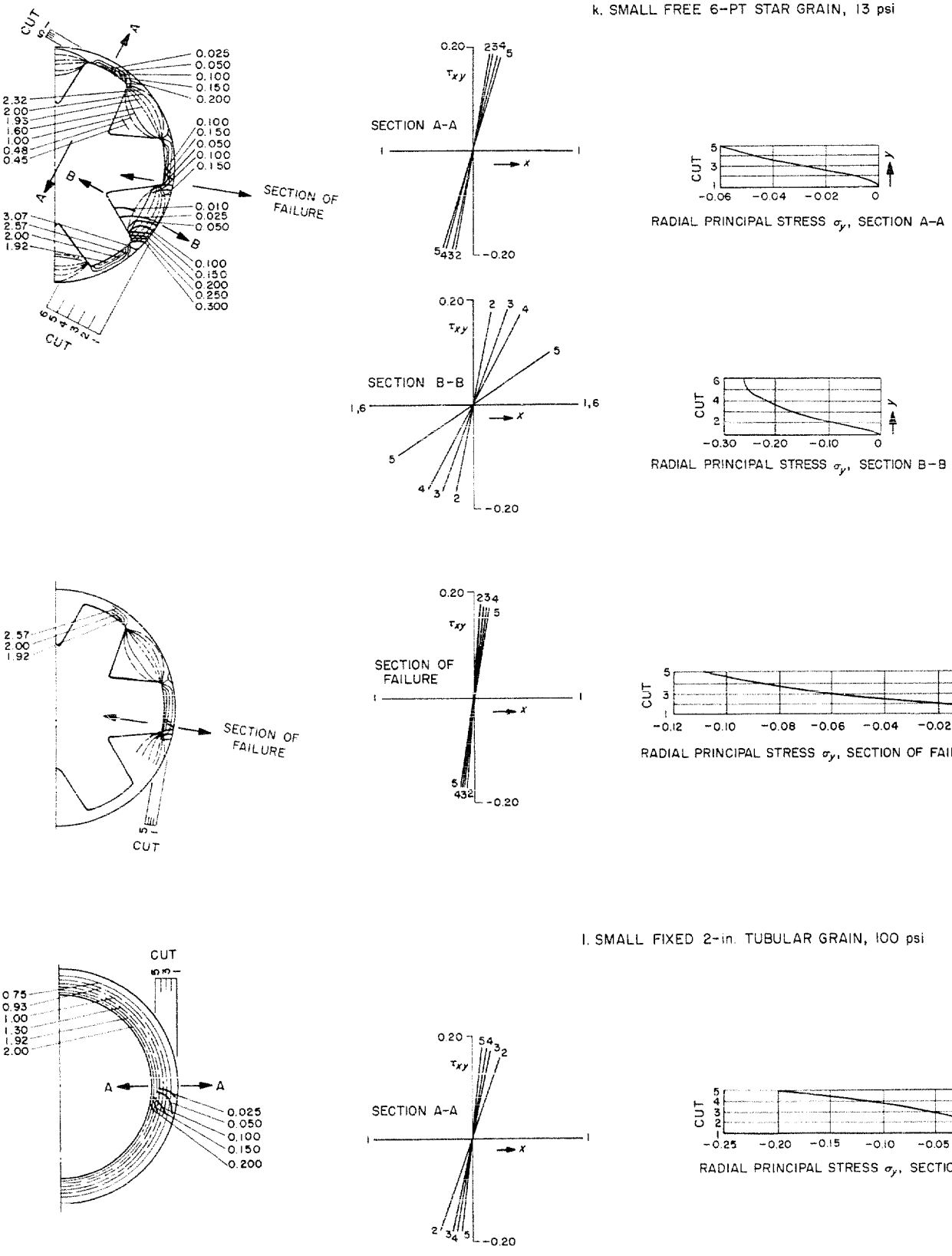

l. SMALL FIXED 2-in. TUBULAR GRAIN, 100 psi

Figure 11. Isochromatic distribution and separation of principal stresses (cont'd)

m. SMALL FIXED 2 1/2-in. TUBULAR GRAIN, 100 psi

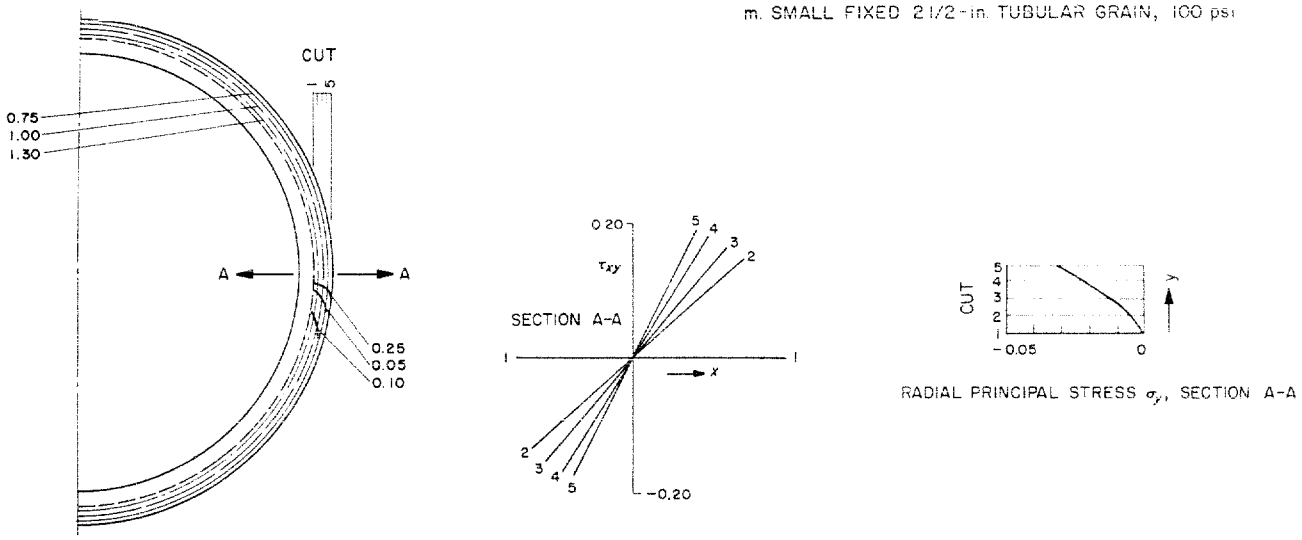

n. SMALL FIXED 4-PT STAR GRAIN, 100 psi

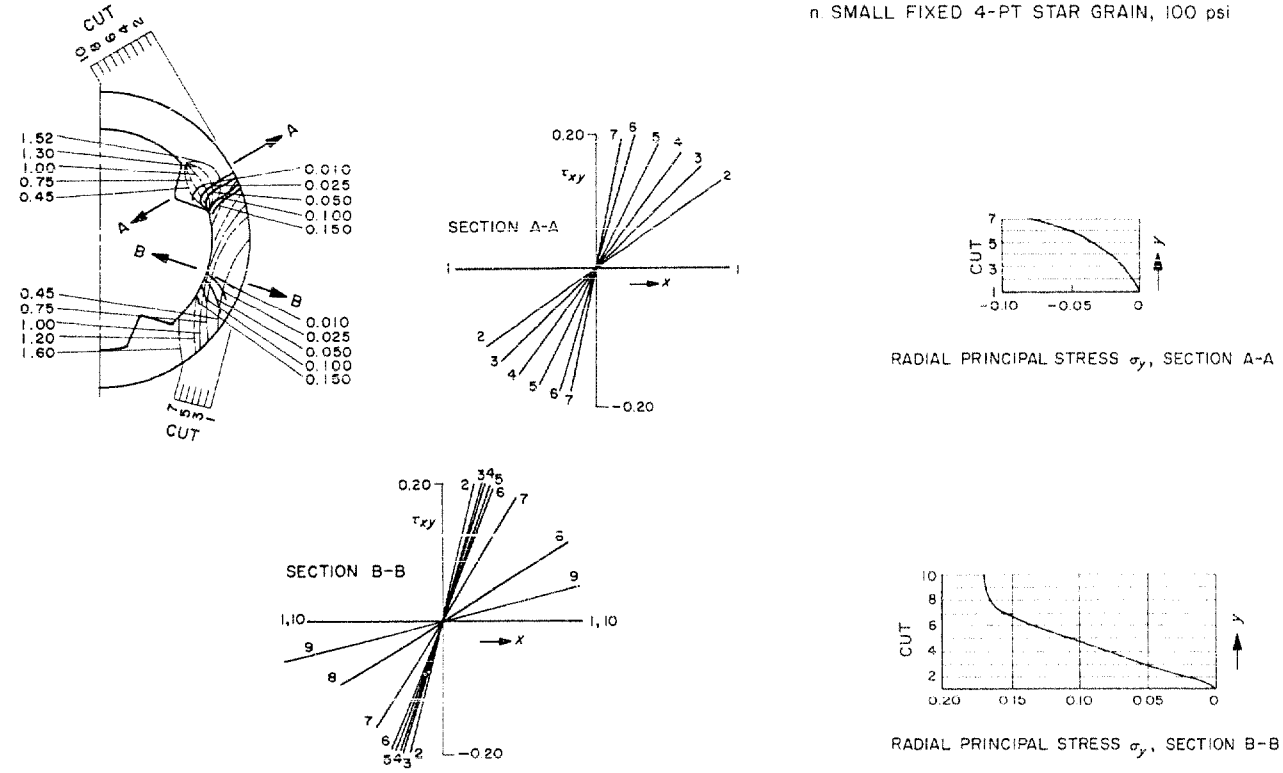

Figure 11. Isochromatic distribution and separation of principal stresses (cont'd)

o. SMALL FIXED 5-PT STAR GRAIN, 100 psi

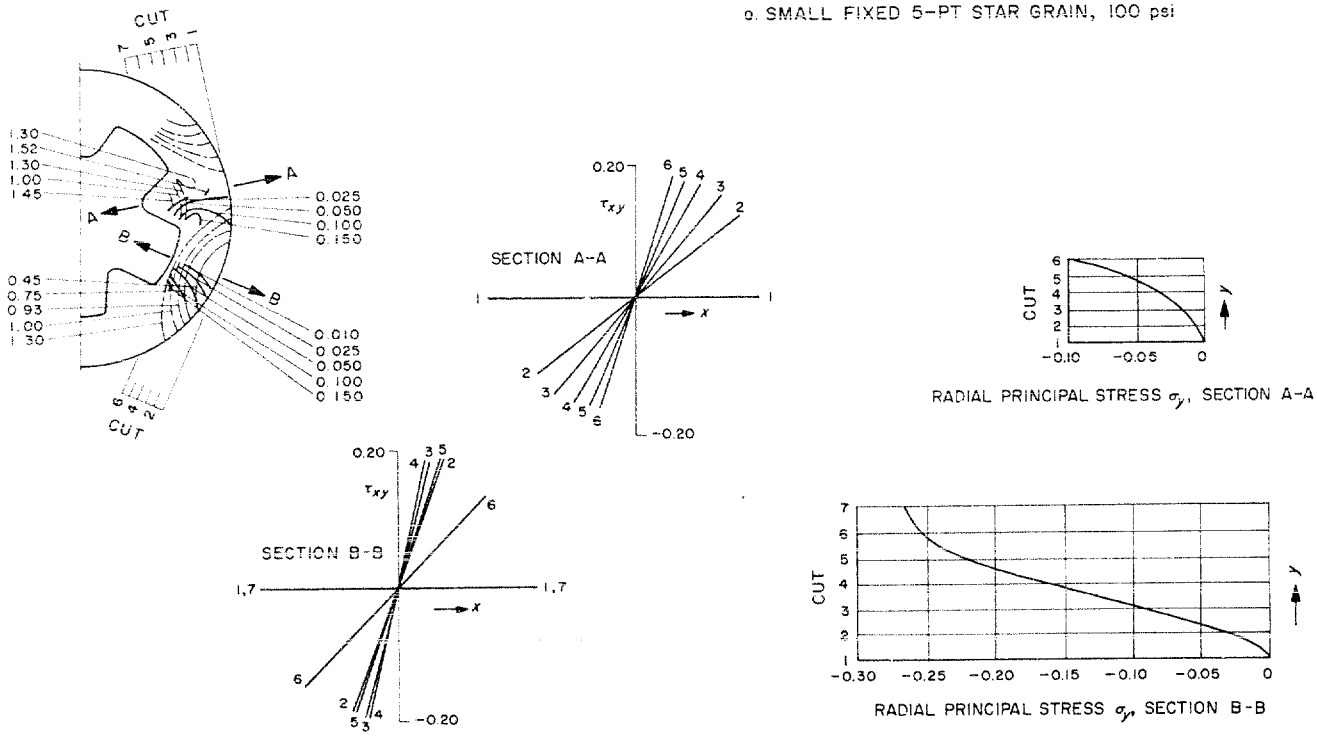

p. SMALL FIXED 6-PT STAR GRAIN, 85 psi

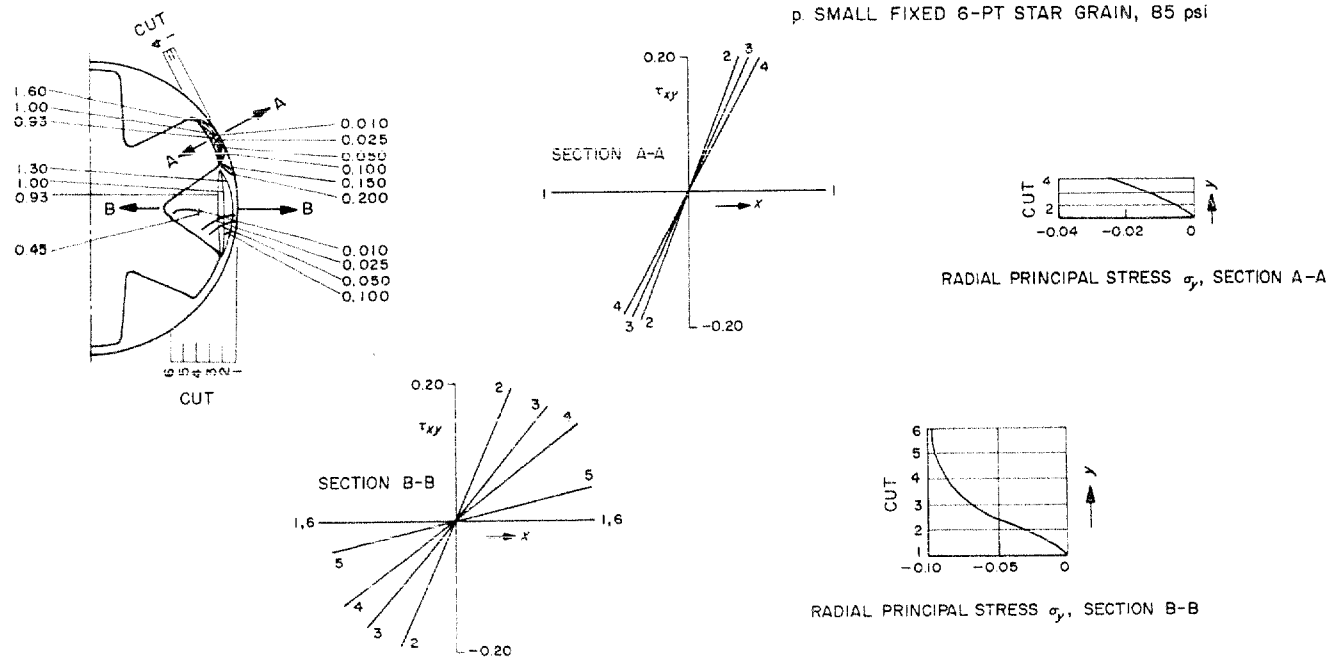

Figure 11. Isochromatic distribution and separation of principal stresses (cont'd)

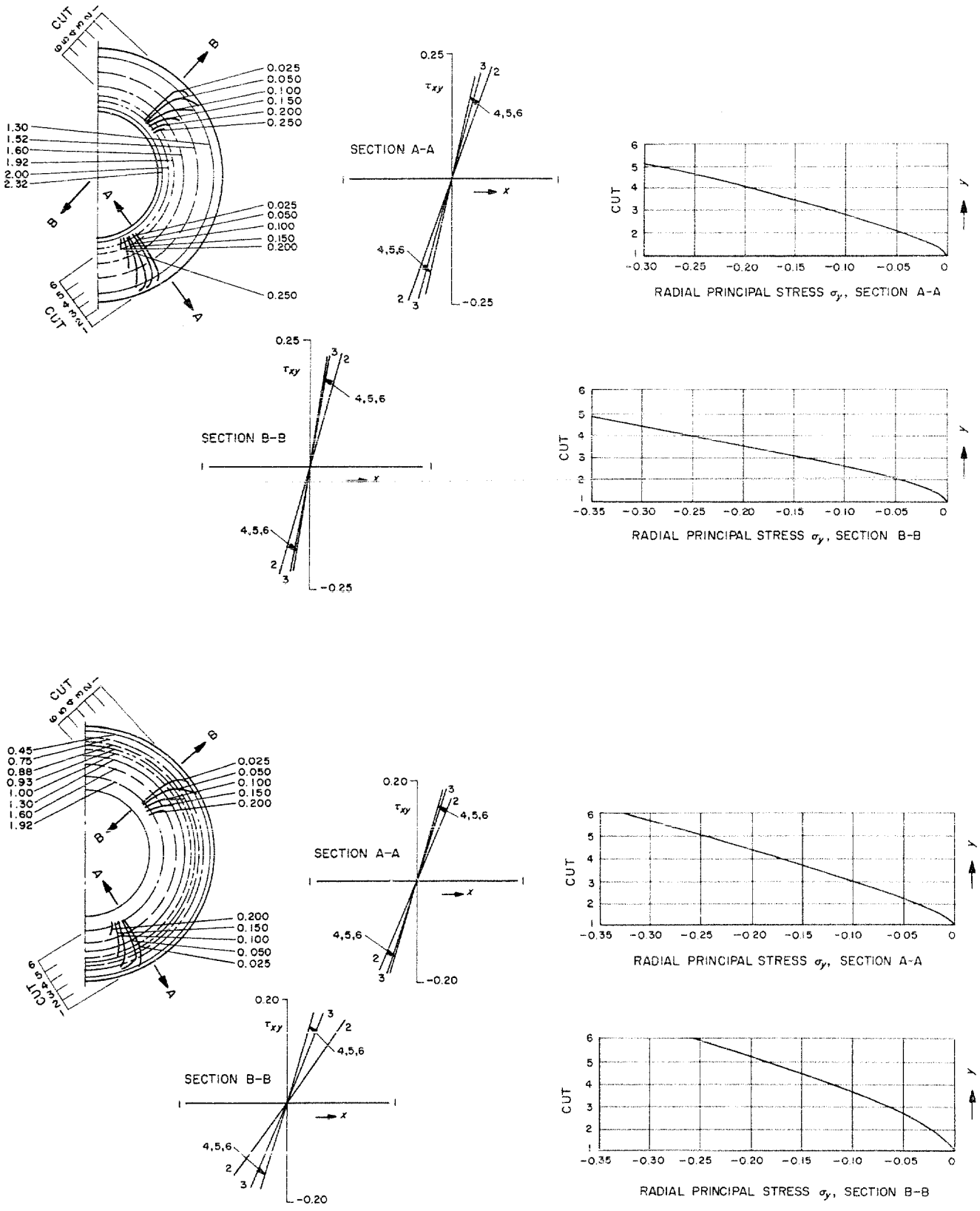

Figure 12. Extreme stress distributions, large fixed and free grains

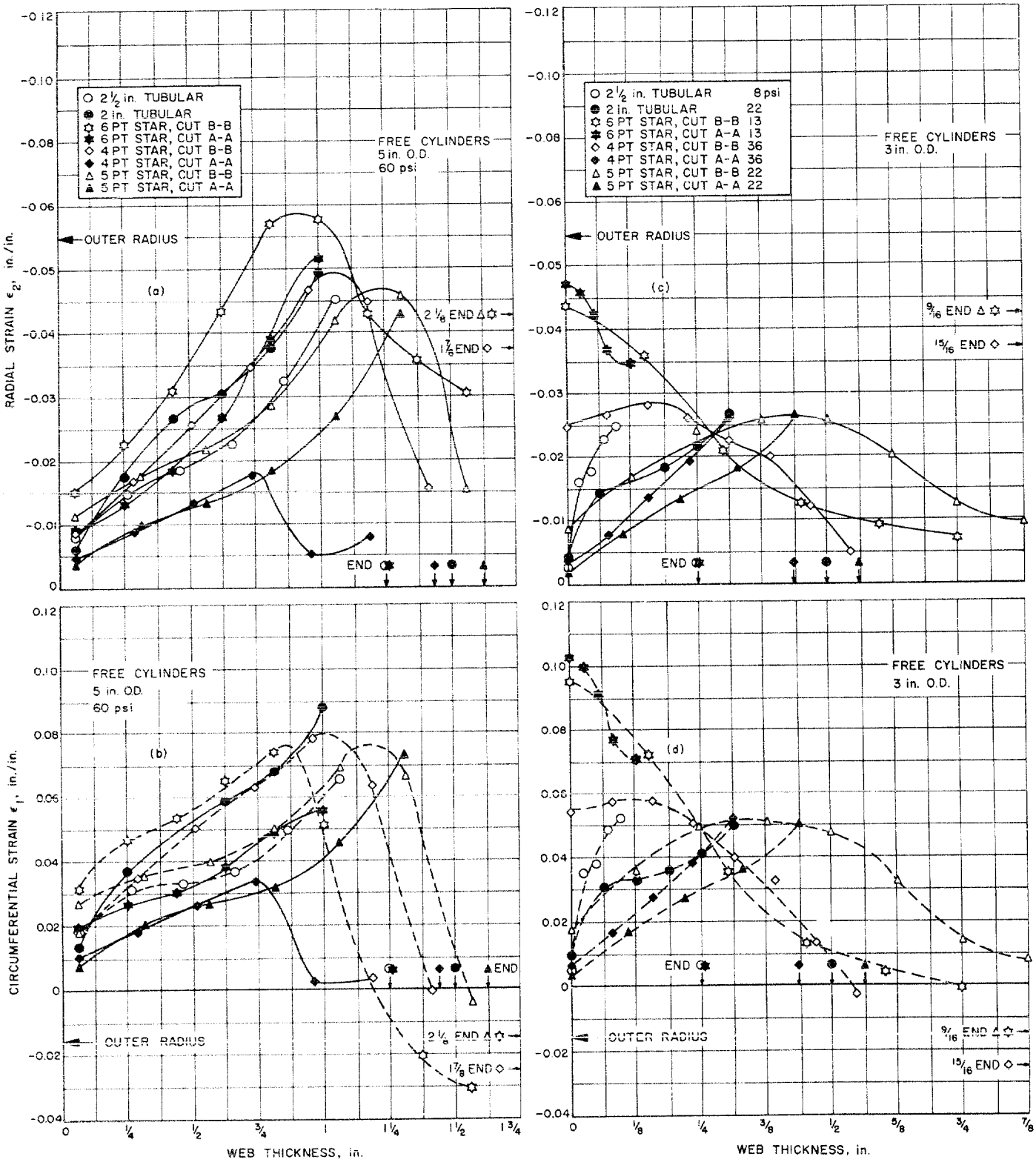

Figure 13. Strain versus web thickness

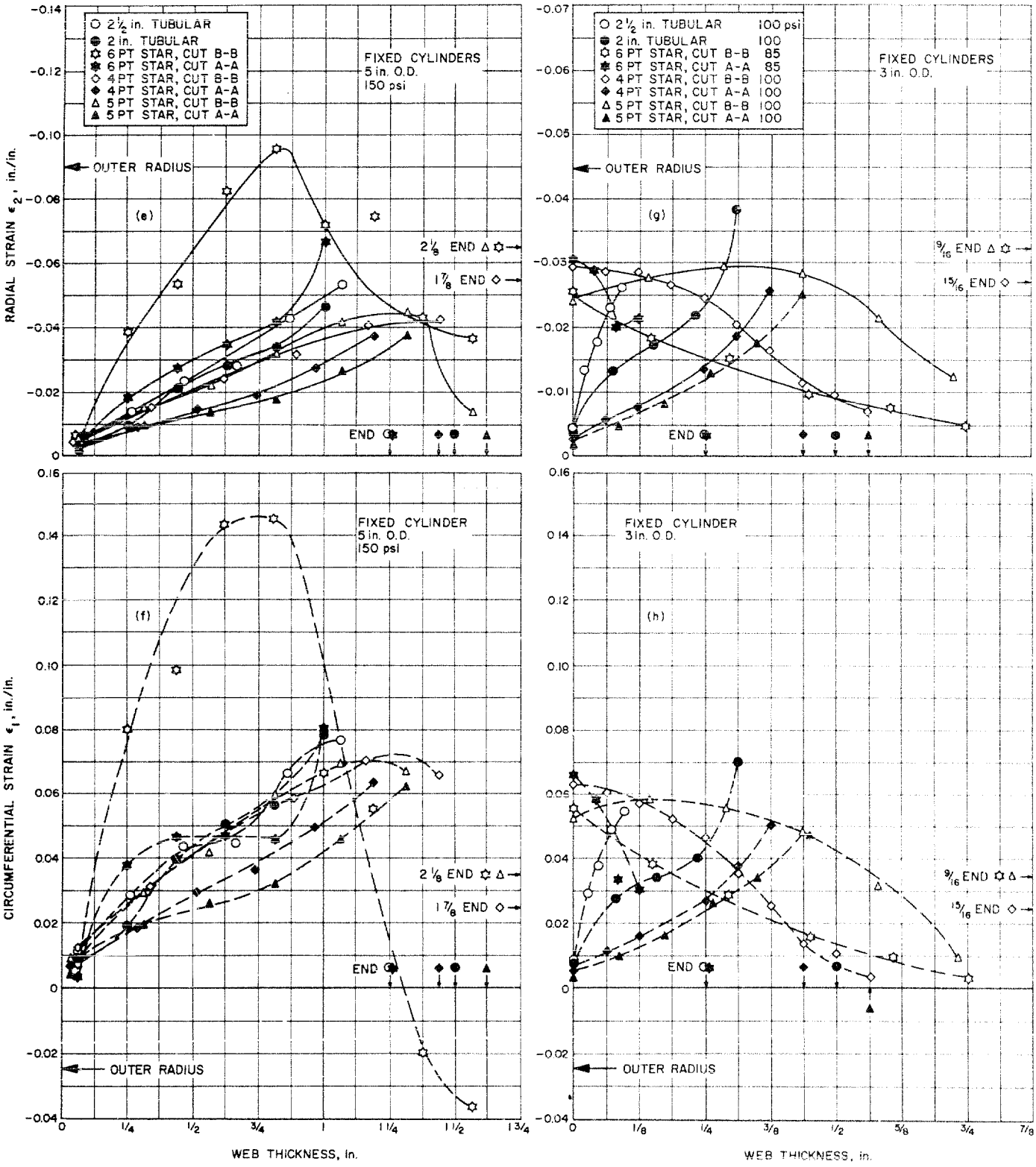

Figure 13. Strain versus web thickness (cont'd)

4. Results and Conclusions

Figures 13a and b record the radial and circumferential strains obtained for the large free grains at 60 psi. Figures 13c and d record the corresponding strains for the small free grains at pressures from 8 to 22 psi.

The largest radial strain (5%) across the web (Section A) occurred in the six-pointed star. The maximum strain existed on the inner surface of the thick web and on the outer surface of the thin web at failure. This seemingly contradictory response may be attributed to material breakdown at failure and thus a corresponding shifting of internal stresses; the failure of the thin web initiated at the outer surface and propagated to the high stress concentration at the root of the star.

The corresponding strains across the web thickness of the large 2½-inch tubular followed essentially the same mode and magnitude as did the large six-pointed star. However, the small 2½-inch tubular strains did not correspond to the large 2½-inch tubular strains in mode or in magnitude compared to the small six-pointed star.

The maximum radial strains in the web of the four- and five-pointed stars were smaller than those for the six-pointed star. This was true for both the large and small grains.

The cut through the star point (Section B) exhibited higher strains than were recorded for the web cut (Section A) in all instances, except at the failure cut in the small six-pointed star. The large strains were observed in the vicinity of the star-point fillets.

Figures 13b and d show that the circumferential strains follow similar distributions as the radial strains. The maximum strains, however, were much larger. Failure of the small six-pointed star occurred at a strain of 10.3% at the outer surface. For the large and small grains, the circumferential strains increased in magnitude along the thick section away from the outer edge. Again, the contradiction (failure at the outer surface with strain gradients increasing toward the interior) may be reasoned by an analogy to the plastic flow theory applied to metal pressure vessels.

In Figures 13e, f, g, and h, the circumferential and radial strains for the plane stressed (fixed) cylinders are shown. What has been stated for the free cylinders can be extended to cover the interpretation of the fixed cylinders; the only differences are that the magnitudes of strains are larger (up to 15%) and the strain concentration factors much more pronounced.

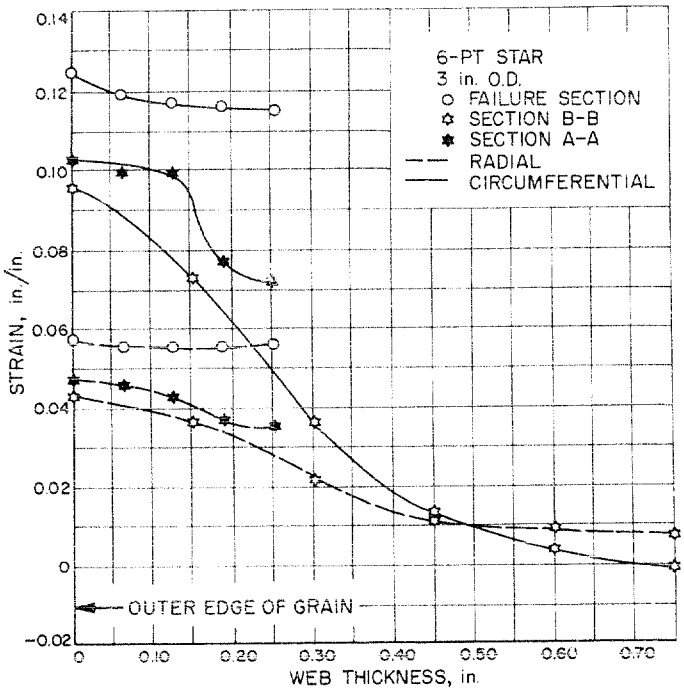

Figure 14. Failure strain, small six-pointed star grain

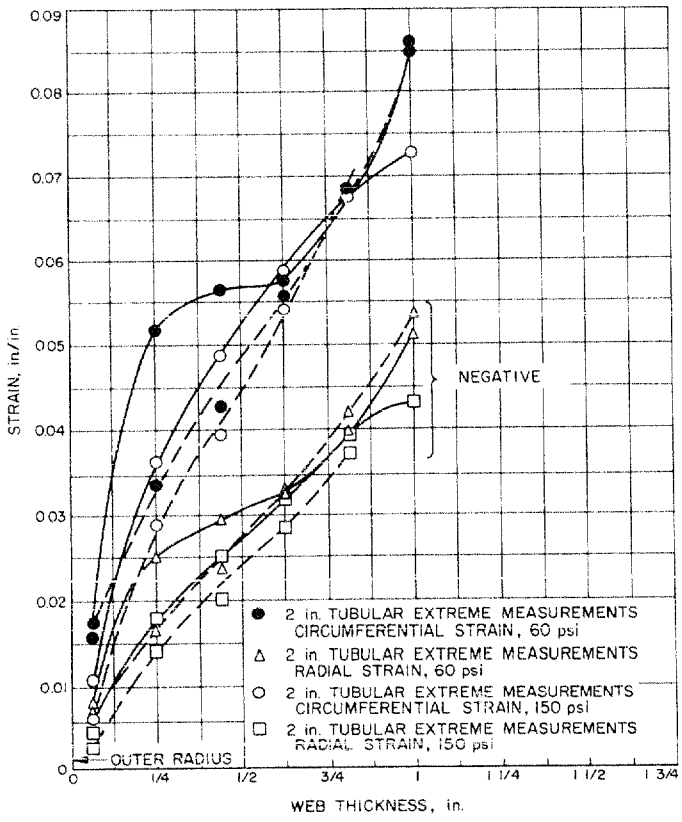

Figure 15. Data-reduction error

Figure 14 gives the strain data at failure for the small six-pointed star. At the failure section the strains are constant: 12% for circumferential strain and 5.5% for radial strain. Note that the grain physical properties of the small cylinders were apparently lower than for the large cylinders due to casting problems.

Figure 15 shows the possible error that may be attributed to any color non-symmetry obtained from the data films. The absolute extremes are shown to be about 25% in error. However, in general, this error is about 10% of the final strain reading. It is believed that by using good judgment in selecting typical sections, this scatter error is less than 5% of the actual strain.

The next program to be initiated will be the mathematical derivation of physical property functions, utilizing presently acquired, as well as future, experimental data. These functions will be general in nature and will inherently contain the biaxial loading effects.

C. Polymer Degradation Mechanisms

J. D. Ingham and N. S. Rapp

The thermal degradation of polymers is being studied to determine the mechanisms of chemical interactions and to investigate the feasibility of developing nondestructive chemical methods for monitoring the extent of degradation and for determining the storage life of solid propellants on the basis of structural chemical changes that may take place. For the present work, an uncrosslinked polyurethane analog of current urethane propellant binders has been prepared from polyoxypropylene glycol (PPG) of molecular weight ≈ 2000 and toluene diisocyanate (TDI, Ref 1).

Preliminary studies have shown that polymer degradation: (1) is substantial at moderate temperatures, (2) is much more rapid in oxygen than in a vacuum or when nitrogen and water vapor are present, (3) appears to proceed more rapidly for small samples, and (4) is profoundly affected by additives, such as ferric acetylacetonate and ammonium perchlorate. At 200°C in a vacuum, CO_2 is the main volatile product, although small amounts of low-mass-number organic fragments are produced. The degradation qualitatively appears to involve a random scission; however, the precise mechanism has not been determined. For example, the types of bonds broken, the importance of weak links, and detailed kinetic measurements have not been carried out.

Since the number of scissions, S, is directly related to the number-average molecular weight, M_n, by

$$M_n(t) = \frac{M_n(0)}{S+1} \tag{1}$$

M_n vs time curves are directly amenable to kinetic analysis. The weight-average molecular weight, M_w, and the viscosity average molecular weight, M_v, depend on the molecular weight distributions produced and, consequently, on the mechanisms. Therefore, comparison of these parameters at various extents of degradation allows a differentiation between possible mechanisms. In addition, plots of molecular weight or volatilization rate versus percentage of volatilization or monomer formation can provide information about the degradation mechanism (Ref 2). A method of fractionation of this polymer has been developed so that M_w, M_n, and the molecular weight distribution may be determined as a function of the extent of degradation. Also, a vacuum balance is being developed for volatilization rate measurements.

1. Fractionation and Molecular Weight Distribution of PPG–TDI Polymers

Large-scale precipitation fractionation of a similar polymer of intrinsic viscosity $[\eta] = 0.33$ dl/gm has been carried out previously (Ref 3), giving a value for the ratio $M_w/M_n = 1.7$, which is close to $M_w/M_n = 2.0$ for the *most probable* distribution expected for condensation polymers. In this work, extraction at 32°C of ≈ 1 gm of polymer coated on glass beads, with isooctane-benzene solvent mixtures successively richer in benzene, have been carried out with reasonable success; however, some degradation occurred during extraction as evidenced by the difference between the initial intrinsic viscosity of $[\eta]_0 = 0.60$ dl/gm and the value of 0.55 dl/gm derived from

$$\frac{1}{W_t}\Sigma_1^i W_i [\eta]_i \tag{2}$$

where

W_t = the total weight

W_i = weight of the ith fraction

$[\eta]_i$ = intrinsic viscosity of the ith fraction

Diphenylpicrylhydrazyl was dissolved in the elution solvents, but degradation still occurred during the fractionation experiments, although independent experiments showed that it inhibited degradation in solution. The

polymer used for these fractionations originally had $[\eta] = 0.71$ dl/gm but had degraded prior to fractionation to 0.60 dl/gm on standing as a benzene solution in a dry box at room temperature.

Results of a typical fractionation from glass beads and one by precipitation from a 4% benzene solution with isooctane precipitant are given in Tables 1 and 2 and Figure 16. The ratio M_w/M_n for the precipitation fractionation was 1.6, which is in good agreement with the value of 1.7 obtained by Moacanin (Ref 3); the column elution fractionation gave a value of 2.2. The discrepancy is probably the result of difficulty in efficiently fractionating the higher molecular weight fractions (>70,000) by precipitation from the relatively concentrated solution.

Table 1. Column fractionation of PPG–TDI polymer

Fraction[b]	Cumulative weight fraction,[c] W_r	Intrinsic viscosity,[d] $[\eta]$, dl/gm	Weight-average molecular weight,[e] M_w
1	0.055	0.127	7,730
2	0.148	0.259	23,400
3	0.239	0.313	31,600
4	0.351	0.420	49,800
5	0.472	0.477	61,400
6	0.592	0.605	88,500
7	0.715	0.631	94,400
8	0.890	0.867	155,600
Original	—	0.600	97,300
Combined	—	0.550	76,300
Column packing: glass beads;[a] recovery = 97.2%; M_w/M_n = 2.24.			
1	0.032	0.159	11,000
2	0.106	0.234	20,200
3	0.195	0.360	39,400
4	0.301	0.463	58,200
5	0.423	0.528	71,600
6	0.547	0.619	92,300
7	0.673	0.785	133,000
8	0.793	1.02	200,000
9	0.924	1.12	222,000
Original	—	0.673	104,500
Combined	—	0.680	106,100
Column packing: Haloport F;[f] recovery = 98.2%; M_w/M_n = 2.14.			

[a] Minnesota Mining and Manufacturing Co.

[b] *Original* refers to whole, unfractionated polymer. *Combined* are corresponding figures calculated from $1/W_r \Sigma_1^r W_i [\eta]_i$, and $1/W_r \Sigma_1^r W_i M_i$; M_i = molecular weight of the ith fraction.

[c] W_r was calculated from $1/W_r [(W_r/2) + \Sigma_1^{r-1} W_i]$.

[d] $[\eta]$ was determined in duplicate and calculated from $\frac{\eta_{sp}}{c} = [\eta] + K'[\eta]^2 c$ using an assumed slope constant of $K' = 0.39$ (Ref 3); c = polymer concentration, gm/dl.

[e] M_w was calculated from $[\eta] = KM^a$, using $K = 4.13 \times 10^{-4}$, and $a = 0.64$ (Ref 3).

[f] F and M Scientific Co.

Table 2. Precipitation fractionation of PPG–TDI polymer[a]

Fraction[b]	Cumulative weight fraction,[c] W_r	Intrinsic viscosity,[d] $[\eta]$, dl/gm	Weight-average molecular weight,[e] M_w
1	0.0345	0.151	10,200
2	0.239	0.388	44,400
3	0.559	0.500	65,600
4	0.735	0.588	84,500
5	0.810	0.696	110,000
6	0.930	0.944	177,000
Original	—	0.570	80,600
Combined	—	0.550	76,100

[a] Footnotes *b*, *c*, *d*, and *e* are given in Table 1.

Notes:
Recovery = 99.8%.
M_w/M_n = 1.62.

A new polymer was prepared and divided into aliquots. These are being stored in bulk under nitrogen at 0°C, and are opened in the dry box and dissolved in benzene just before use. A fractionation was run using Haloport F (a vapor phase chromatography substrate believed to consist of teflon particles) as the column packing. In this case, the $[\eta]_0 = 0.673$; the value calculated from Expression (2) was 0.680. The ratio of M_w/M_n was 2.14, in agreement with fractionations from glass beads (Table 1 and Fig 16). The constancy of the distribution in going from an Expression (2) value of 0.68 to 0.55 dl/gm is significant, since this indicates that the initial degradation is random and that $[\eta]$ may be used for kinetic measurements at small extents of bond scission.

2. Development of a Vacuum Balance

Although the literature (Refs 4 and 5) describes numerous vacuum microbalances, most of them are difficult to construct (requiring elaborate alinement jigs) or, as in the case of helical balances, are very load-limited.

For the present studies, a simple and rugged double pan balance has been constructed. The beam consists of a 2- by 150-mm length of steel syringe tubing rigidly attached to a perpendicular crosspiece of 6- by 25-mm quartz tubing. The ends of the quartz tube have been closed to ≈0.5 mm by heating. The beam is supported at the quartz tube by passing a 3-mil tungsten wire through the end holes and connecting it at the ends to support posts. The balance is placed inside a bell jar on a vacuum base plate. The tube to the vacuum pumps and a vertical connecting tube are attached to the base plate. The connecting tube is closed at the lower end and heated by means of a refluxing vapor bath.

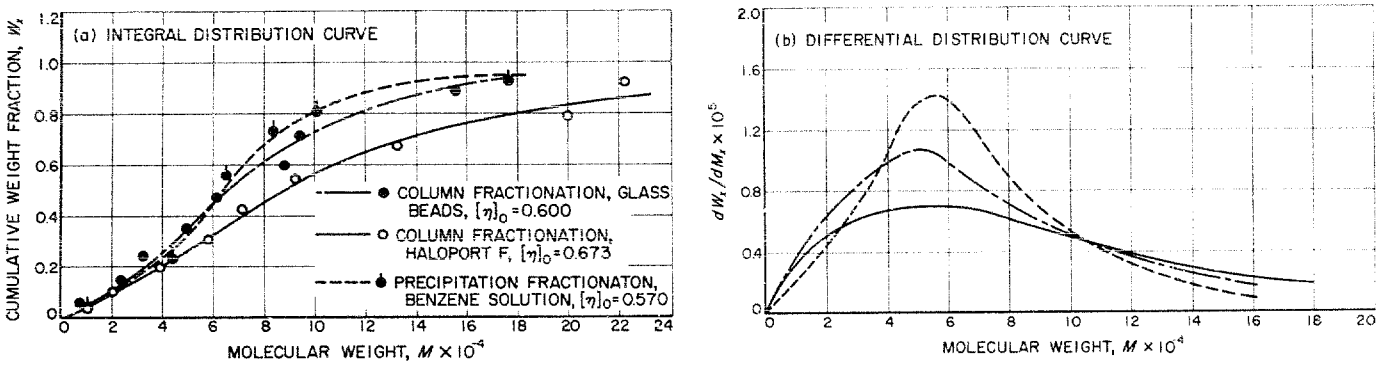
(a) INTEGRAL DISTRIBUTION CURVE
CUMULATIVE WEIGHT FRACTION, W_z
MOLECULAR WEIGHT, $M \times 10^{-4}$
COLUMN FRACTIONATION, GLASS BEADS, $[\eta]_0 = 0.600$
COLUMN FRACTIONATION, HALOPORT F, $[\eta]_0 = 0.673$
PRECIPITATION FRACTIONATON, BENZENE SOLUTION, $[\eta]_0 = 0.570$
(b) DIFFERENTIAL DISTRIBUTION CURVE
$dW_z/dM_z \times 10^5$
MOLECULAR WEIGHT, $M \times 10^{-4}$

Figure 16. Fractionation of PPG–TDI polymer

The sample is placed in a 0.5-gm platinum container attached to one end of the beam and suspended through the vacuum-system base-plate opening into the heated tube; a similar pan is attached to the opposite end of the beam as a counterweight. The deflection of the end of the beam is read on a steel scale placed inside the bell jar and read with a magnifying glass. The scale reads to 0.01 inch, and the balance sensitivity is 0.037 inch or 0.94 mm per mg; therefore, it can be read directly to 0.27 mg and estimated to 0.03 mg.

Preliminary data are given in Figures 17 and 18 for PPG of molecular weight 2000 and compared with data obtained on atactic PPG of molecular weight 16,000 obtained by Madorsky and Straus (Ref 6). The discontinuities in the upper curve for PPG of molecular weight 2000 (Fig 17) were caused by disturbing the vacuum system. The discontinuity in the lower curve was believed to be caused by sticking. The apparent initial rates are within a factor of two of that determined by Madorsky and Straus based on a somewhat arbitrary extrapolation of their data to zero time (Fig 19). However, in the region of 20 to 40% weight loss, where the data can be compared directly, the rates agree remarkably well, considering the large differences in apparatus, sample size, polymer preparation, and initial molecular weight. The increase in rate above 30% volatilization observed in the present experiments may reflect evaporation of residual polymeric fragments as the polymer is degraded to relatively low molecular weight.

The balance design will be improved to eliminate discontinuities in the rate curves and to obtain a moderate increase in sensitivity.

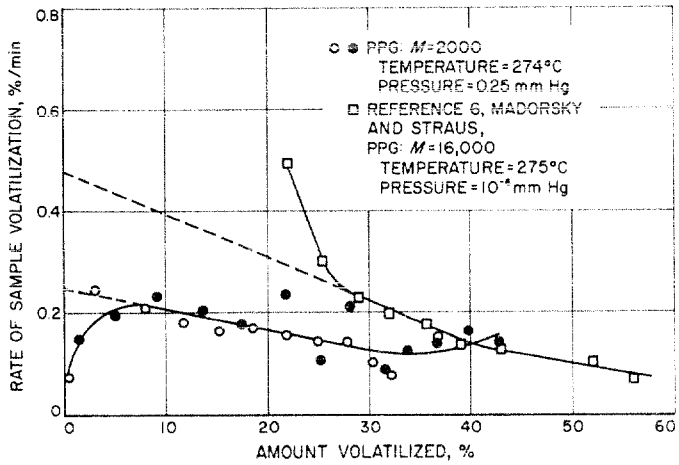

Figure 18. Rate of thermal degradation of PPG

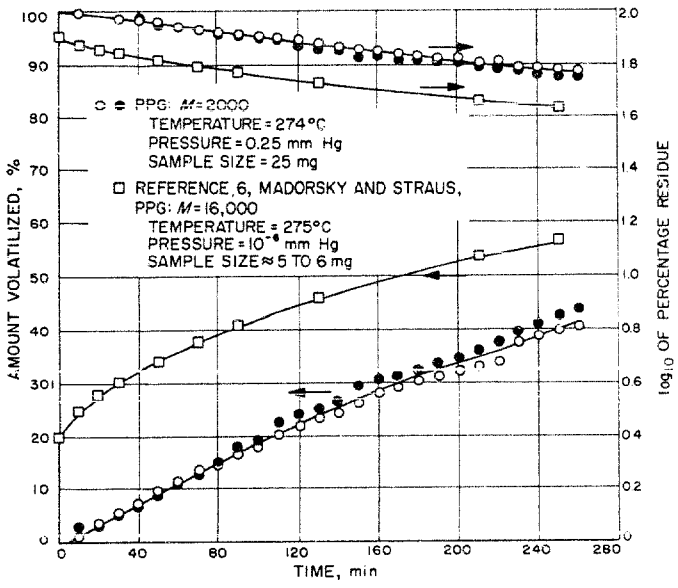

Figure 17. Thermal degradation of PPG using a vacuum balance

3. Kinetic Interpretation of Degradation Curves

Although a rigorous kinetic treatment of the degradation curves given in Figure 21 of Reference 1 requires determination of the molecular weight distributions versus time, preliminary analysis can be carried out if several reasonable assumptions are made:

(1) The molecular weight distribution is normal and does not change during the degradation, where the degradation process is random.

(2) The degradation reaction is first order with respect to polymers.

(3) The relationship $[\eta] = K\bar{M}_v^a$ is valid throughout the degradation.

(4) The unit chain length can be estimated.

Data are shown in Figure 19, assuming unit-average chain lengths, $m = 1087$, where scission occurs at the urethane bonds; and $m = 63$, assuming scission can occur at ether or urethane bonds. Derivation of the integrated form of the rate equation

$$-\ln\left(\frac{N_n - 1}{N_n}\right) = -\ln\left(\frac{N_{n(0)} - 1}{N_{n(0)}}\right) + kt$$

where N_n is the number-average chain length, is given in Reference 2. A plot of $-\ln[(N_n - 1)/N_n]$ vs time should give a straight line if the assumptions are valid. In oxygen, the degradation process appears to be autocatalytic as expected. In the absence of oxygen, the extent of degradation is too small relative to the scatter of points to clearly establish that the process is first order. The absence of weak links is apparent, since extrapolation of the curves to zero time gives a number-average chain length which is the same as the initial chain length. This is in contrast with the results for hydrolytic degradation of poly-(ether)-urethanes (Ref 7), in which extrapolation of $-\ln[(N_n - 1)/N_n]$ to zero time gives a value for N_n much less than the initial chain length.

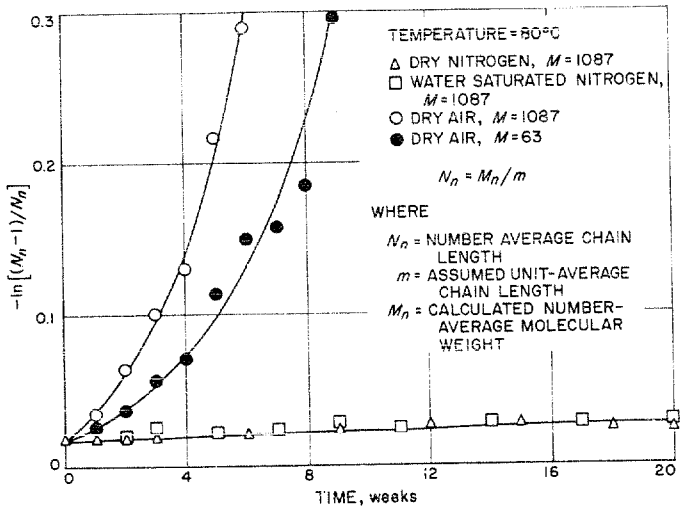

Figure 19. Degradation of PPG–TDI polymer

References

1. *Quarterly Summary Report No. 38-4*, Jet Propulsion Laboratory, Pasadena, California, July 15, 1961.

2. Grassie, N., *Chemistry of High Polymer Degradation Process*, Butterworths Publications, London, 1956.

3. Moacanin, J., "Diisocyanate-Linked Polymers. 1. Dilute Solution Properties of Toluene Diisocyanate-Extended Polypropylene Glycol," *Journal of Applied Polymer Science*, Vol 1, pp 272–282, 1959.

4. Katz, M. J. (editor), *Vacuum Microbalance Techniques*, Plenum Press, Inc., New York (1961).

5. Madorsky, S. L., "Rates of Thermal Degradation of Polystyrene and Polyethylene in a Vacuum," *Journal of Polymer Science*, Vol 9, p 133—156, 1952.

6. Madorsky, S. L., and Straus, S., "Thermal Degradation of Polyethylene Oxide and Polypropylene Oxide," *Journal of Polymer Science*, Vol 36, pp 183–194, 1959.

7. Morton, M., and Harwood, H. J., *Degradation Studies on Condensation Polymers*, Institute of Rubber Research, University of Akron, Akron, Ohio, January 14, 1961.